



Instrument Science Report WFC3 2009-21

WFC3 SMOV Results: IR Channel Dark Current, Readnoise, and Background Signal

B. Hilbert & P. R. McCullough
15 August 2009

ABSTRACT

Using data taken during Servicing Mission Orbital Verification (SMOV), we have characterized basic dark current and readnoise behavior of the IR Channel, along with its level of measured background signal. Unless otherwise indicated, results in this report refer exclusively to those obtained during SMOV program 11447, with the IR FPA temperature of -128 C. The correlated double sampling (CDS) read noise in RAPID sequences is 20-22 electrons, similar to that measured in TV3 (Hilbert 2008), and comparable to the Contract End Item (CEI) Specification, 21.2 electrons. The effective noise measured in an image created from 16 reads of a SPARS200 ramp is 11.6 – 12.7 electrons. The dark current measured from SPARS200 ramps is 0.043 – 0.050 $e^-/s/pixel$, again better than the CEI specification of $<0.4 e^-/s/pixel$, with a goal of 0.1 $e^-/s/pixel$.

Introduction

WFC3 began SMOV testing of its cooled IR detector in mid-June 2009. Program 11447, “IR dark current, read noise, and background,” was designed to benchmark those characteristics of the IR detector using internal observations for the darks and externals for the backgrounds. This report summarizes a cursory analysis of data from program 11447, including measurements of read noise, dark current, and the IR background

(actually foreground) sky at two locations (the HST orbital pole and the anti-solar direction) for a variety of illuminations of the Earth below the HST.

Program 11447 executed in June, July, and August 2009. All data were obtained with in full-frame mode with MEB2 as usual, using Science Mission Specifications (SMSs), i.e. no real time commanding. The temperature of the IR detector was -127.9 C (145.1 K) and constant to within 0.2°C throughout program 11447. All data were obtained at the nominal “2.5 e/ADU” setting, although the measured (inverse) gain is a bit different than the eponymous value. Gain values used for these analyses were derived from SMOV data taken as part of the IR Functional Test (proposal 11420). Details are given in Hilbert (2009). Gain values for the four quadrants (following the usual convention of quadrant 1 in the upper left, with quad numbers increasing in the counter-clockwise direction) are 2.33, 2.28, 2.45, and 2.47 e/ADU.

Data

Each of visits 1-20 consists of full-frame imagery: a RAPID-6 followed immediately by a SPARS200-15 and another RAPID-6. We refer to these as “darks” and from these we obtain dark current, read noise, and reference pixel behavior.

Visit 33 collected one full frame ramp through each of the wide- and medium-band filters while pointing in the anti-sun direction. Visit 34 repeated these observations while pointed at the orbit pole. The purpose of these observations was to measure the background levels through each filter. Characteristics of the data collected under this proposal are given in Table 9.

All data were run through CALWF3 for basic data reduction. This included reference pixel subtraction, zeroth read subtraction, cosmic ray rejection, and non-linearity correction for the background observations. We only made one change to the default behavior of CALWF3 when processing these data. For both dark current and internal flat field ramps, CALWF3 is run with the UNITCORR keyword set to OMIT. We processed the data for this proposal with UNITCORR set to PERFORM. This causes the output **flt.fits* files to be in units of ADU/sec and have values that are normalized to the appropriate exposure time for each pixel. If UNITCORR is not set, the **flt.fits* files are output in units of ADU, and for each pixel, contain the signal value present at the final unrejected read. This leads to an image that essentially has a variable exposure time from pixel-to-pixel and is not useful for analysis purposes. By turning UNITCORR to PERFORM, our output **flt.fits* files contained appropriate signal rates. Tables 10 and 11 in Appendix 1 list the reference files used by CALWF3 for its processing steps.

The first four Visits of this proposal were potentially subject to the same light leak that was observed in the IR Functional Test data (Hilbert 2009). For these Visits, the darks were collected with the channel select mechanism (CSM) in the IR position, meaning that any light incident upon the WFC3 pickoff mirror was directed to the IR channel. Despite having the aluminum BLANK in place for the dark current

observations, rather than a filter, a small fraction of incident light reached the IR detector. Using the same “bright Earth” plots shown in Hilbert (2009) and described in McCullough (2009), we were able to identify dark current ramps taken while HST was pointed down at the day side of the Earth. Figure 1 shows this “bright Earth” plot for the SPARS200 dark ramp collected in Visit 2. From this plot we see that HST was pointed down at the day side of the Earth (filled yellow squares) for almost the entire 2800 seconds of the exposure (which spans between the vertical green line and the vertical dashed red line).

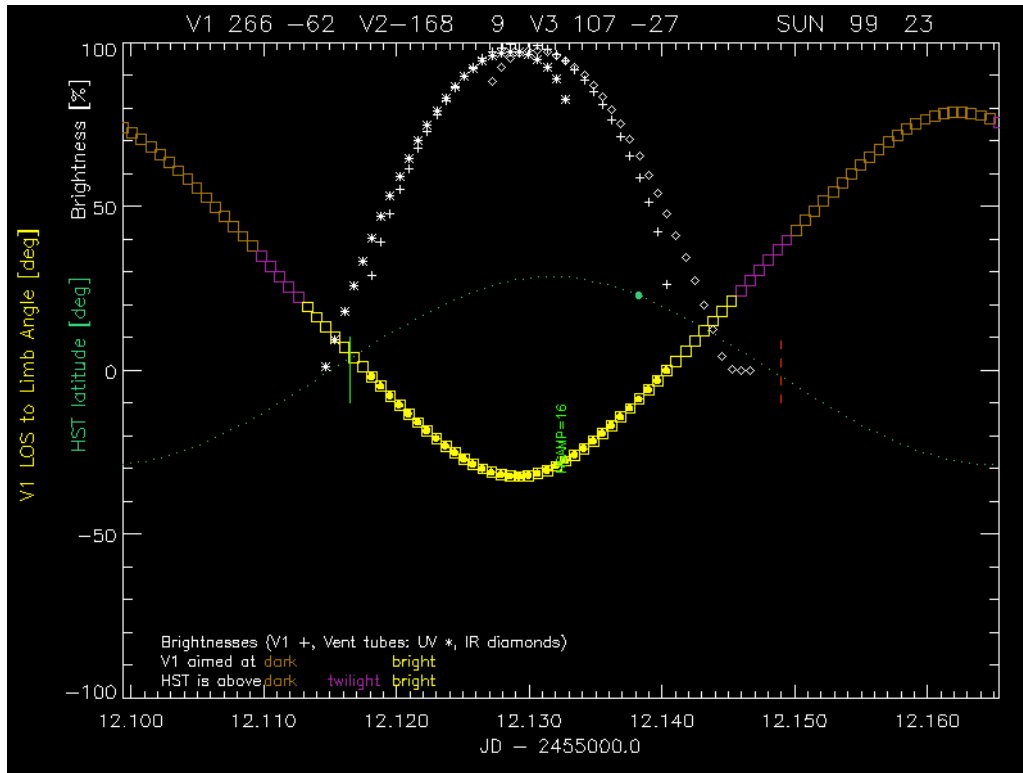


Figure 1: Plot of HST's pointing direction for the Visit 2 SPARS200 ramp. The filled yellow squares indicate the time during which HST was pointed down at the day side of the Earth (V1 to limb angle < 0), while the vertical green line and vertical dashed red line indicate the beginning and ending times of the exposure.

Figure 2 shows the mean signal in each read of that Visit 2 SPARS200 ramp. As predicted, the mean signal (red points) increases much more quickly than in an uncontaminated dark current ramp (blue points), and also increases in a non-linear fashion as HST crossed the day side of the Earth, with its varying brightness due to clouds/ocean/land etc. After examination of all ramps in the dataset, we found two of the SPARS200 ramps and one RAPID ramp contaminated by light leak. These SPARS200 ramps were ignored for the purposes of calculating dark current rate. The exposure time

of the RAPID ramp was small enough that the light leak had a negligible effect on the measured readnoise.

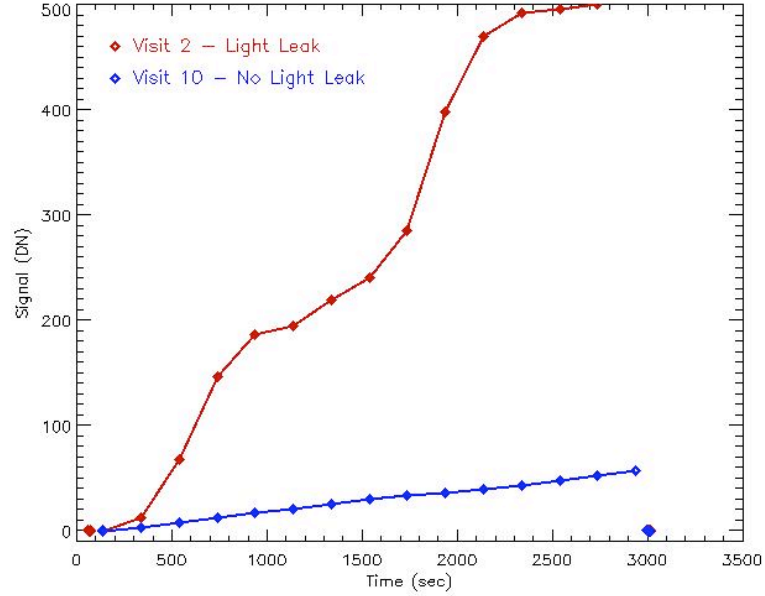


Figure 2: Mean signal up the ramp for a ramp affected by light leak (red) while looking at the bright Earth, versus a ramp taken while looking at the bright Earth after the CSM fix was in place (blue).

Beginning with Visit 5, a remedy to the light leak was put in place. From this point on, all IR dark current observations were made with the CSM in the UVIS position. This means that any light incident upon the WFC3 pick-off mirror was directed to the UVIS side of the instrument rather than the IR side. Figure 3 shows an image of the final read of an uncontaminated SPARS200 dark current ramp (Visit 12). The image is a histogram equalization stretch, from 0.0 (black) to 0.4 e/s/pixel (white). Figure 4 shows a surface plot of the dark current rate for the same image.

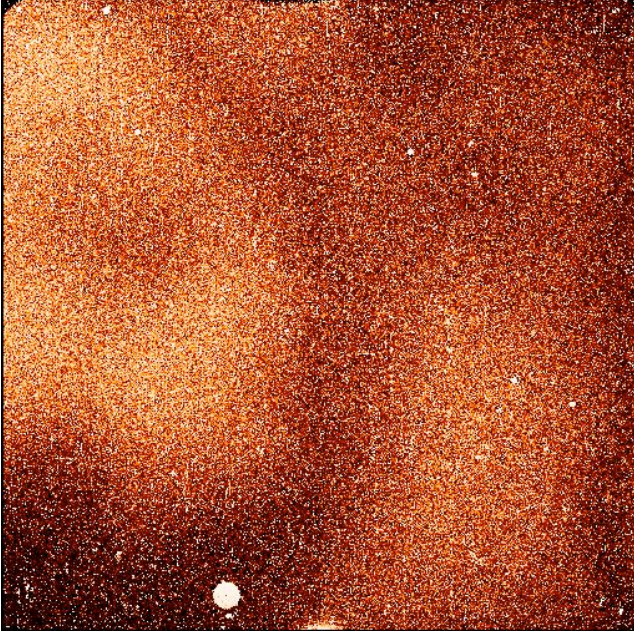


Figure 3: Dark current image from Visit 12 SPARS200 ramp. Histogram equalization stretch between 0 and $0.4 e^-/\text{sec}/\text{pixel}$.

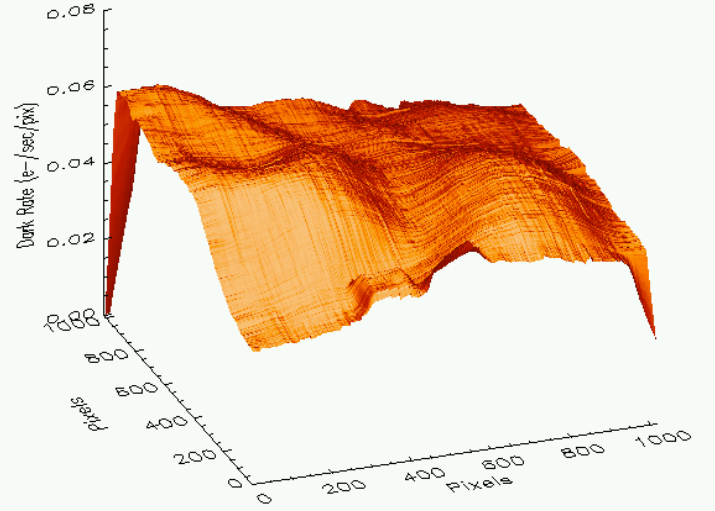


Figure 4: Surface plot of the dark current image to the left.

Analysis

Bias Level

Our first analysis task was to monitor the bias level of all of the dark current ramps, in order to search for any patterns. We obtained a measure of the bias level of each ramp by calculating the sigma-clipped mean in the zeroth read of each ramp. This was done prior to any CALWF3 processing. Figure 5 shows the mean signal in the science pixels of each quadrant for the 60 ramps taken in Visits 1-20 of this proposal. Similarly, Figure 6 shows the sigma-clipped mean values of the reference pixels in each quadrant. Each Visit contained three ramps. Visits are plotted in alternating blue and red points, for clarity.

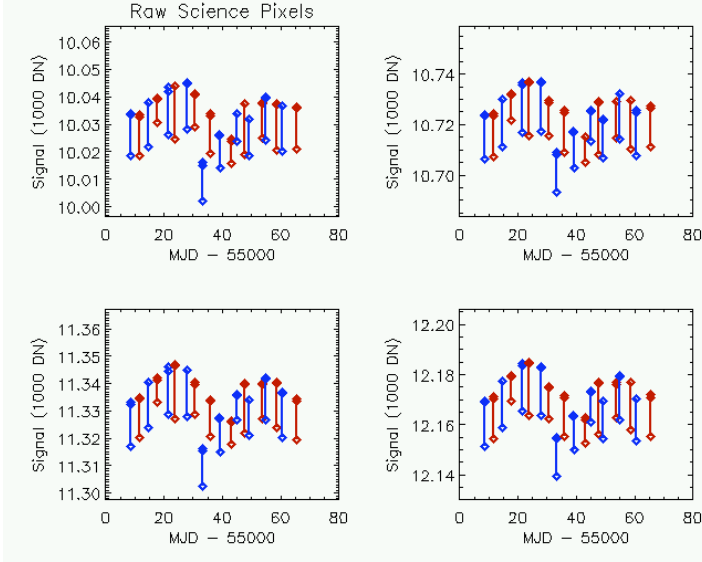


Figure 5: Mean signal in the science pixels of each quadrant for the zeroth read of all 60 dark ramps. Each Visit consisted of 3 ramps. Visits are plotted in alternating colors for clarity.

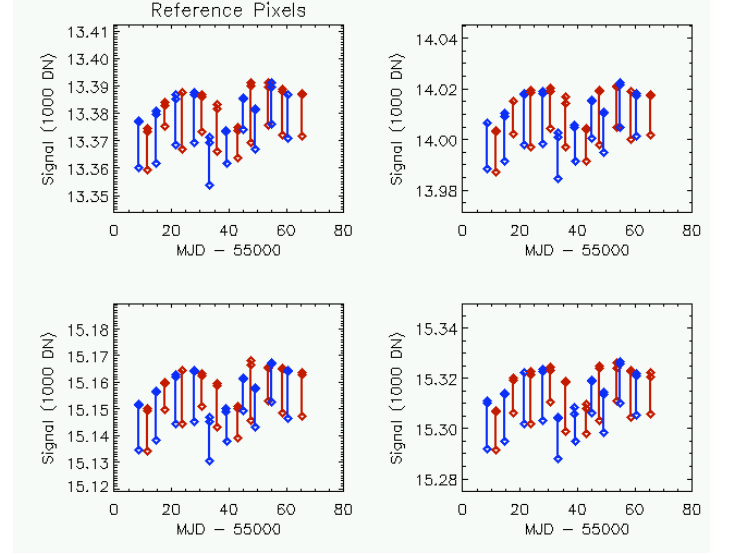


Figure 6: Mean signal in the reference pixels of each quadrant for the zeroth read of all 60 dark ramps.

These figures show that the raw bias level in both the science and reference pixels varies by 40 to 50 DN over a timescale of days. The similarity in the patterns between Figures 5 and 6 suggests that upon reference pixel subtraction, this pattern should be removed.

To better show the behavior on a shorter timescale, Figures 7 and 8 show the same plots as Figures 5 and 6, but zoomed in to cover only Visits 11 through 14. Here we see that the first two ramps in each Visit (the initial RAPID, followed by the SPARS200) have very similar bias levels. However, the third ramp in each Visit (also a RAPID) consistently has a bias level 15 – 20 DN below the previous two ramps. The exact cause behind this is not understood, although Figures 9 and 10 show that this effect is largely corrected through reference pixel subtraction.

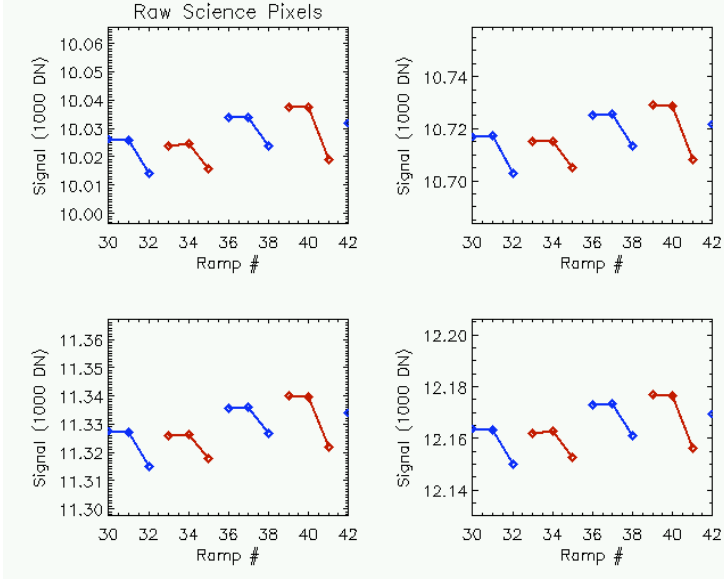


Figure 7: Same as Figure 5, expanded to show Visits 11 through 14. Each Visit shows similar mean signals in the zeroth read for the first two ramps. The mean signal third ramp is ~ 15 to 20 DN lower.

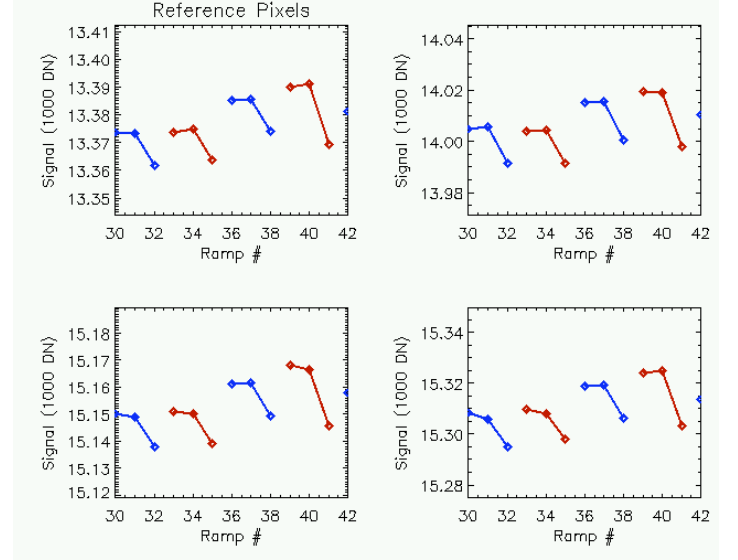


Figure 8: The mean reference pixel values for Visits 11 through 14. The reference pixels show a similar pattern to the science pixels.

One of the processing steps performed by CALWF3 is reference pixel subtraction. The information shown above will be invisible to WFC3 users unless they examine the raw ramp files of their observations. In the *ima* and *flt* files of their data, bias levels will be removed through reference pixel subtraction. We next subtracted the reference pixel values shown in Figure 6 from the science pixel values in Figure 5. The result is shown in Figures 9 and 10. Curiously, a long timescale pattern in the bias level remained after reference pixel subtraction. There appears to be a linear decrease with time in the reference pixel subtracted zeroth read level. Using a robust line-fitting algorithm, we find that the signal level in the four quadrants is decreasing by 0.21 to 0.25 DN per day. Uncertainties associated with the line-fitting are 0.02 DN per day. The deviation of the signal in Visits 8 and 9 (low signal points) from this overall trend is also not understood.

Figure 10 shows the same information, but zoomed in to cover Visits 11 through 14. The overall decrease in zeroth read level is not as obvious here because we plot versus ramp number rather than time, due to the long time between Visits. Here we see no consistent pattern among the three ramps in each Visit. The third ramp is not systematically lower than the first two, as it was in Figures 7 and 8. Variations in the mean signal level are now 5 DN at most.

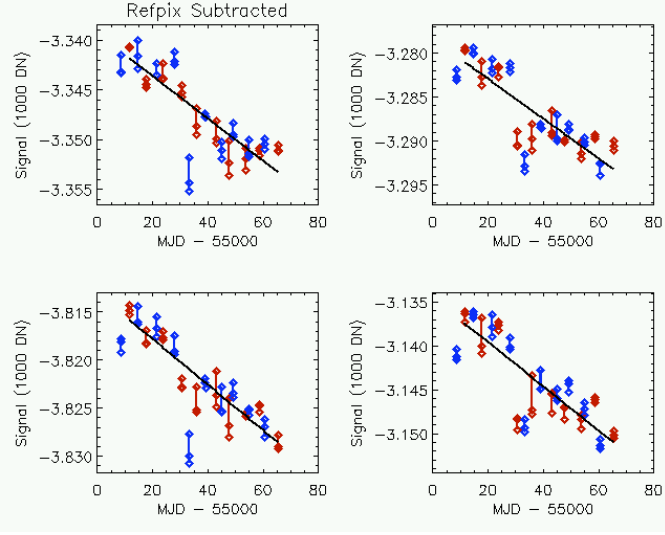


Figure 9: Reference pixel subtracted mean signal levels in the zeroth reads of all 60 dark current ramps.

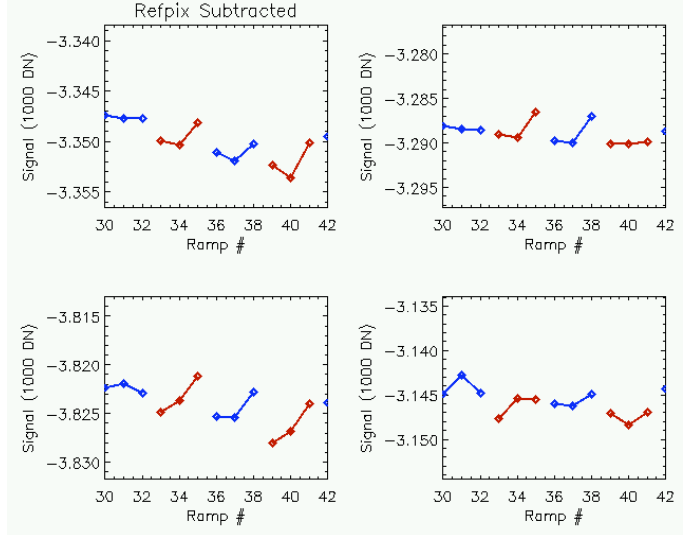


Figure 10: Enlarged version of Figure 9, showing Visits 11 through 14.

During the second round of ground testing, we monitored a dark current rate that varied with the temperature of the focal plane (Hilbert 2008a). Despite the fact that FPA temperature control greatly improved during TV3 and these variations were no longer seen (Hilbert, 2008c), we checked these data for any correlation between the bias level and the temperature. Figure 11 shows the mean bias level as well as the FPA temperature for the SPARS200 ramps in this dataset. Figure 12 zooms in on the three Visit 14 ramps. The measured detector temperature measured by the thermistor jumps up and down only one step over the entire duration of these observations. Therefore, we are limited by the resolution of the thermistor and can see from these plots that we are unable to find any correlation between FPA temperature and bias level.

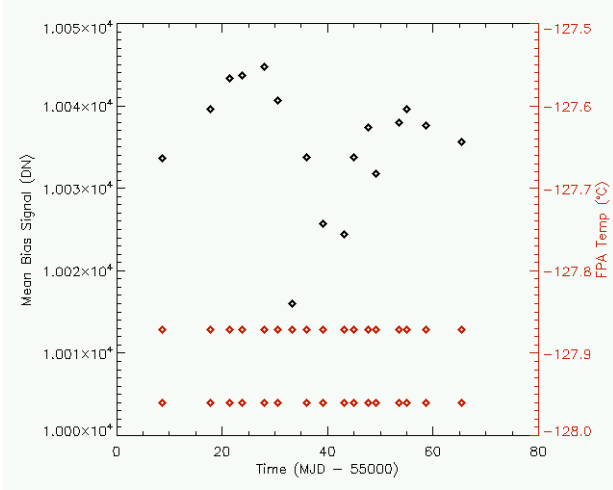


Figure 11: Mean signal in the zeroth read for all SPARS200 darks, along with FPA temperature values.

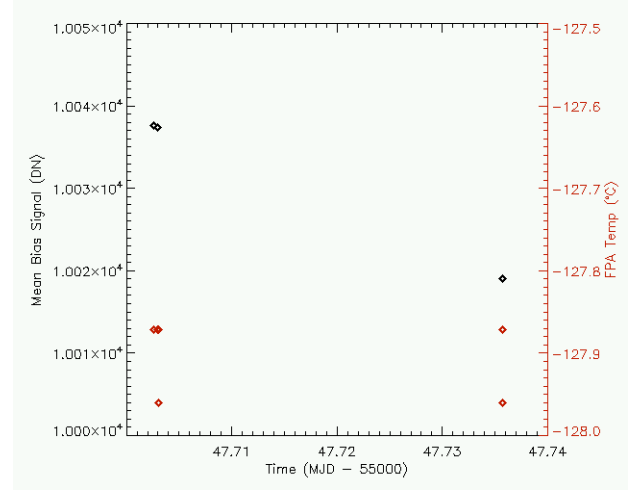


Figure 12: Mean signal in the zeroth read for Visit 14, with accompanying FPA temperature values.

After analyzing the bias levels in these dark current ramps, we moved on to analysis of the mean signal levels going up the ramps. First, we calculated the sigma-clipped mean signal in each of the four quadrants for every read of every ramp. The results for the SPARS200 ramps are plotted in Figure 13. These plots show a surprising variation of the mean signal in a set of nominally identical ramps.

In an effort to filter out ramps that may be subject to persistence effects, we identified IR observations taken prior to each Visit in this proposal. Three Visits with potential contamination above nominal dark current were identified, and are shown in red as having higher-than-expected dark current, in Figure 13. During Visit 4, HST was pointed down at the night side of the Earth. This Visit occurred prior to the CSM fix, meaning these ramps could have been subjected to the same light leak effects explained above. While HST was pointed at the night side of the Earth for Visit 4, there is still the possibility of HST pointed at a bright artificial light. Visit 8 began approximately 2 hours after a set of internal flat field observations, suggesting persistence as the culprit for its high dark current. Similarly, Visit 19 darks were collected only 25 minutes after a set of internal flat field observations.

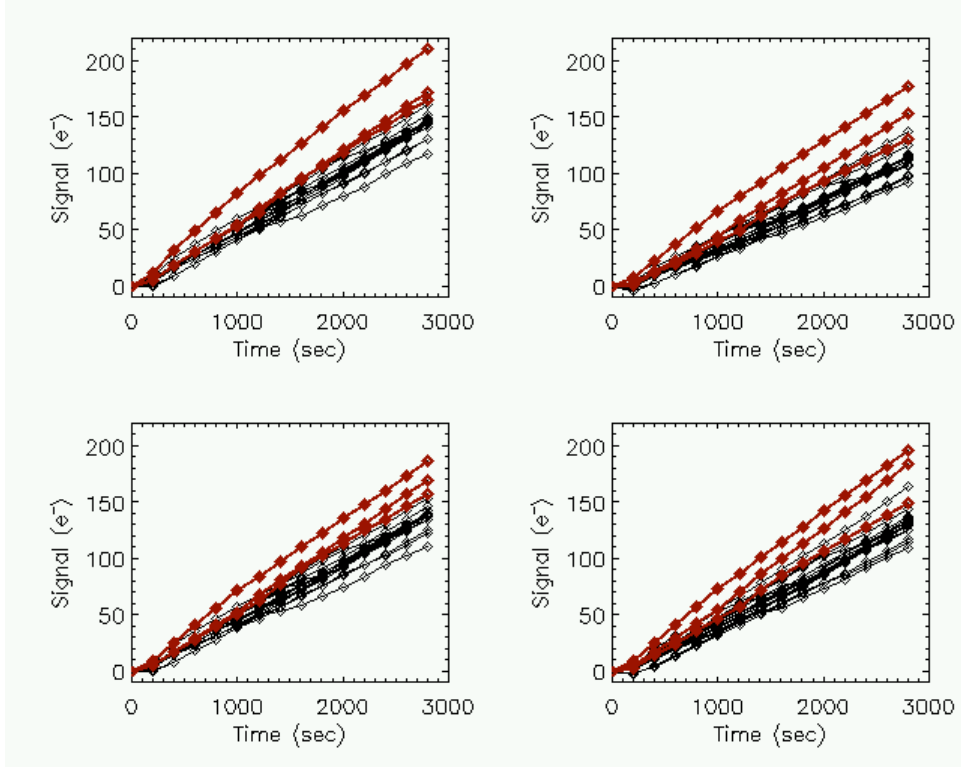


Figure 13: Mean signal up the ramp for all SPARS200 dark current ramps in this proposal. Visits 4, 8 and 19, which showed the largest dark current values in Figure 22, are shown in red.

Robust standard deviation of the signal values in read 15 of the black curves in Figure 13 is 43 – 48 e^- for the four quadrants. With measured signals of 100 – 150 e^- , we expect a noise of $\sim 25 e^-$ from the combination of readnoise and shot noise from the dark current. This implies that we have a source of noise beyond shot noise and readnoise present in these data.

Readnoise

As was done with TV3 data, as well as data from proposal number 11420, we calculated two measures of noise for the IR channel from the data taken in this proposal. (Hilbert, 2008b) The first is CDS noise, and the second is “effective noise”. CDS noise is the measure of the standard deviation in a difference image created from two consecutive reads within a ramp, while effective noise provides a measure of the noise after all reads of a ramp have been combined to form a final image.

CDS and effective noise values were calculated using the same method as was used on TV3 data. Results from that test are detailed in (Hilbert, 2008b). CDS readnoise values were calculated using the RAPID-15 dark current ramps taken in Visits 1 through 20. The second RAPID ramp from Visit 3 suffered from light leak. However, due to the short exposure time of the RAPID sample sequence, the effect on the measured readnoise

was minimal, as seen in Figure 14. For each 15 read ramp, we created 14 difference images using consecutive reads. We then created a histogram of the values in each difference image, and performed a Gaussian fit in order to calculate the width (Gaussian sigma, using Markwardt's *mpfitpeak.pro*¹) of the histogram. This provided a measure of the total noise in the difference image. However, this measured noise included contributions from both the read noise and shot noise from dark current signal. In order to remove the dark current contribution to the noise, we first determined the dark current in each pixel by fitting a line to that pixel's signal through the 15 reads of the ramp. The slope of this line gave us the dark current rate for that pixel. We then multiplied this rate by the exposure time between two consecutive reads in the ramp. For the case of the RAPID ramps, this was 2.9 seconds. This gave the total dark current signal that accumulated between the two reads. The square root of this signal is the dark current shot noise contribution. By subtracting the square of the dark current noise (ie the dark current signal) from the square of the total measured noise from the histogram fitting, and taking the square root of the result, we obtained a measure of the true CDS readnoise. For short ramps, like RAPIDs, the subtraction of the dark current shot noise has no significant effect on the measured readnoise. However for longer ramps, there is a noticeable effect. We repeated this calculation on all 14 difference images for a given ramp, and then took the median of these values as the CDS readnoise for that ramp. Figure 14 shows the CDS readnoise values calculated for all RAPID ramps in this proposal, and Table 1 reports the mean readnoise values for the dataset.

¹ Available at <http://www.physics.wisc.edu/~craigm/idl/fitting.html>

Copyright (C) 1997-2001, 2003, 2005, 2007, 2008, 2009, Craig Markwardt

This software is provided as is without any warranty whatsoever. Permission to use, copy, modify, and distribute modified or unmodified copies is granted, provided this copyright and disclaimer are included unchanged.

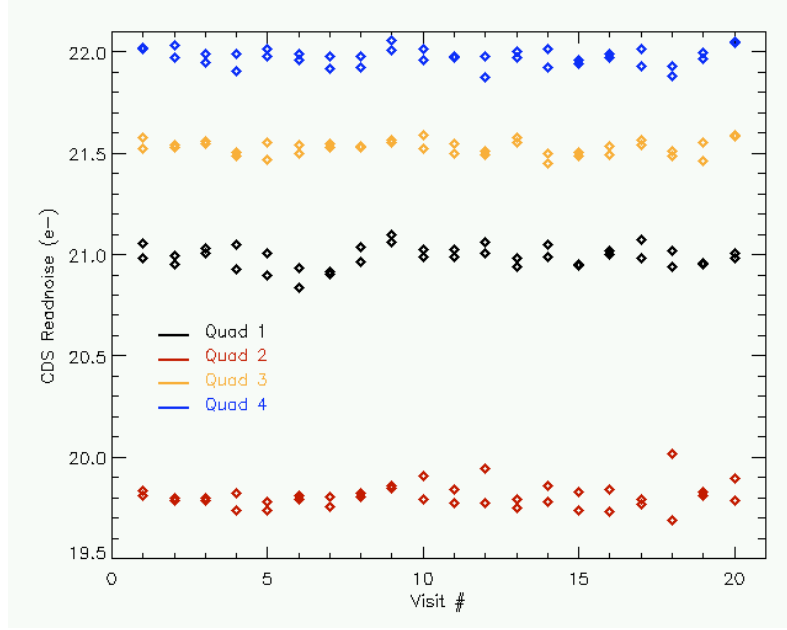


Figure 14: CDS readnoise values measured for the 2 RAPID ramps per Visit in Visits 1 through 20. Table 1 presents the sigma clipped mean for each quadrant. Values are identical to those measured in SMOV program 11420.

We converted the values from ADU to electrons with the mean SMOV gain values derived from data taken as part of SMOV program 11420 (Hilbert, 2009). The CDS readnoise values derived from this dataset, as well as from the proposal 11420 dataset, are reported in Table 1. The readnoise values agree to within the uncertainties for all four quadrants. For comparison, we also show the CDS readnoise values measured in TV3 testing, where we have converted the values given in Hilbert (2008b) to the SMOV gain values. For all 4 quadrants, the CDS readnoise values from SMOV testing are comparable to those from ground testing.

By the same process we evaluated CDS read noise for the SPARS200-15 ramps and report those values in Table 1 also. For these longer ramps, light leak was more of a concern. For the purposes of calculating noise values, we ignored the SPARS200 ramps from Visits 2 and 3, as they were contaminated by light leak effects. Again, the SMOV CDS readnoise values are similar to those calculated in TV3. Due to the long exposure time between reads (200 seconds) other sources of noise push the measured CDS readnoise of the SPARS200 ramps above that of the RAPID ramps.

CDS Readnoise (e^-)				
	Quadrant 1	Quadrant 2	Quadrant 3	Quadrant 4
SMOV – RAPID this proposal	20.99 +/- 0.05	19.80 +/- 0.05	21.53 +/- 0.04	21.98 +/- 0.04
SMOV – RAPID Proposal 11420	21.03 +/- 0.02	19.87 +/- 0.04	21.53 +/- 0.03	21.99 +/- 0.04
RAPID TV3 (converted to SMOV gain)	20.8	20.0	21.8	22.0
SMOV - SPARS200 this proposal	22.21 +/- 0.09	21.16 +/- 0.10	22.78 +/- 0.08	23.13 +/- 0.06
SMOV – SPARS200 proposal 11420	22.39 +/- 0.29	21.33 +/- 0.17	23.08 +/- 0.16	23.41 +/- 0.06
TV3 SPARS200	22.2	21.4	22.8	23.2

Table 1: CDS readnoise values measured in SMOV versus those measured in TV3 ground testing. For ease of comparison we took the TV3 values presented in Hilbert (2008a) and converted them to the SMOV gain values measured in this proposal. The uncertainty on the CDS measure for a single SMOV ramp was $0.06 e^-$. Ten RAPID ramps were averaged together to give the values in this table. The uncertainties given are the robust standard deviation of the set of readnoise measurements. For the SPARS200 ramp, the stated uncertainties are the robust standard deviations of the readnoise values measured for all CDS pairs up the ramp.

The second type of noise calculated from these data was effective noise. This is a measure of how well the noise averages down in a given ramp compared to the number of reads used to create a final image. Similar calculations were performed on ground testing data, the results of which are detailed in Hilbert (2008b). In order to calculate the effective noise for a ramp, we begin by fitting a line to the signal in each pixel up the ramp. This is the same method that CALWF3 uses to create a final image (stored in the flt file) from a data ramp (stored in the ima file). By multiplying the formal uncertainty in the best-fit slope by the exposure time of the ramp, we arrive at a measure of the noise associated with that pixel in the final image. We then create a histogram of these effective noise values and fit a Gaussian to the distribution in order to determine the position of the peak. The histogram peak positions are the values reported in Table 2 and shown by the four curves in Figure 15. By varying how many reads of the ramp we use in the line-fitting, we are able to determine the effective noise in ramps of any length.

Figure 15 shows the mean measured effective noise calculated from all of the SPARS200 ramps. The line for each quadrant (one color per quad) shows the measured effective noise versus the number of reads used to create the final image. We see that when using all 16 reads (corresponding to NSAMP=15 plus the zeroth read) the final image has an effective noise of 11.6 to 12.7 e^- .

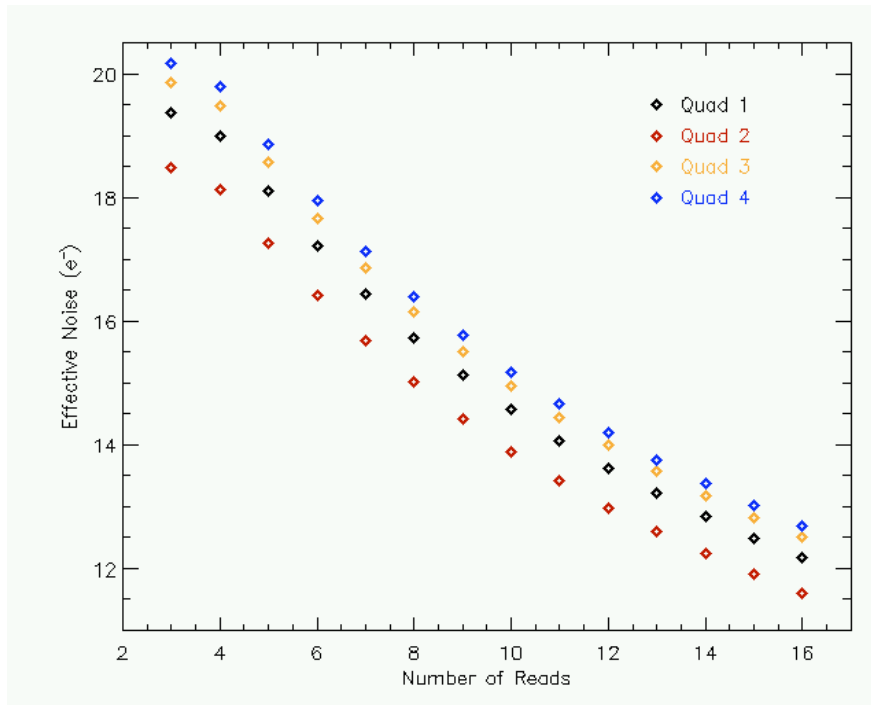


Figure 15: Mean effective noise versus the number of reads for the SPARS200 ramps.

Figures 16 through 18 show the effective readnoise for each SPARS200 ramp when using all 16 reads to create a final image. The sigma-clipped means and standard deviations of these values are listed in Table 2, with values calculated during TV3 testing for comparison (Hilbert 2008b). As was seen in the IR Functional Test for SMOV (Hilbert 2009), the mean effective noise measured on orbit is consistently lower than that from ground testing.

Close inspection of the effective noise values in quadrants 3 and 4 of Figure 16 reveals that in several of the Visits, the effective noise did not average down as expected, leading to points outside the range of the plot. Figures 17 and 18 show zoomed out views of the effective noise for quadrants 3 and 4. While the two quadrants show high noise values in several common Visits, there are other high noise Visits that exist only in one quadrant.

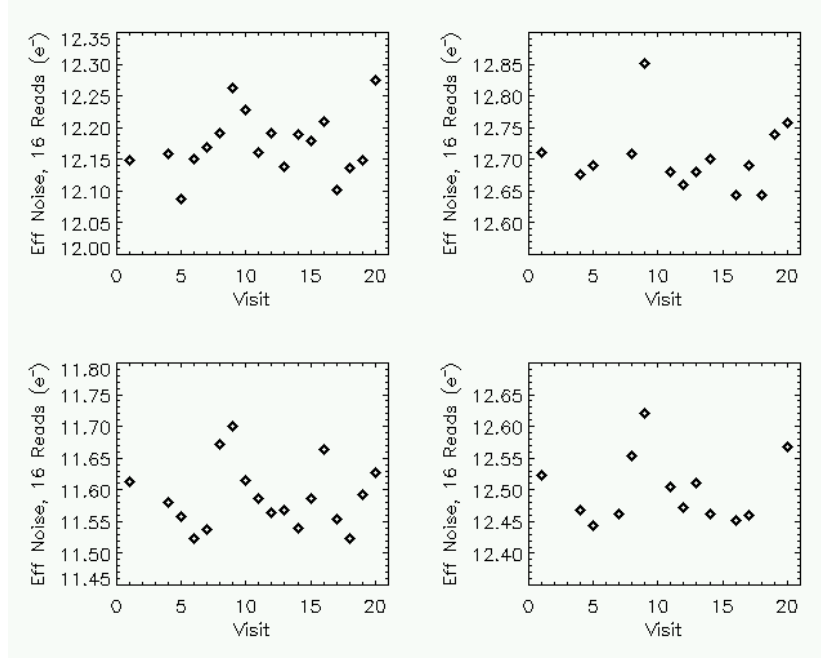


Figure 16: Effective noise when using all 16 reads of a SPARS200 ramp, for each visit. Note that for several ramps, the effective noise in quadrants 3 and 4 is above the range of the plot. A zoomed out view is given below.

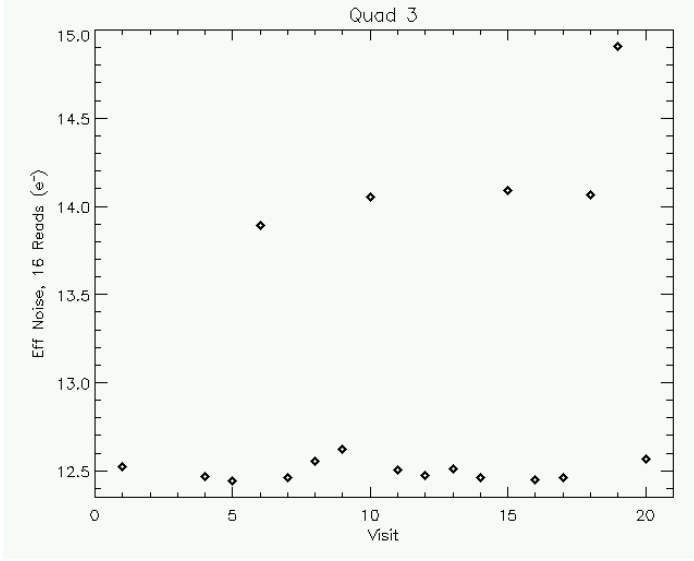


Figure 17: Zoomed out view of quadrant 3 in Figure 16. The effective noise in five of the Visits fails to average down in the same way as the others.

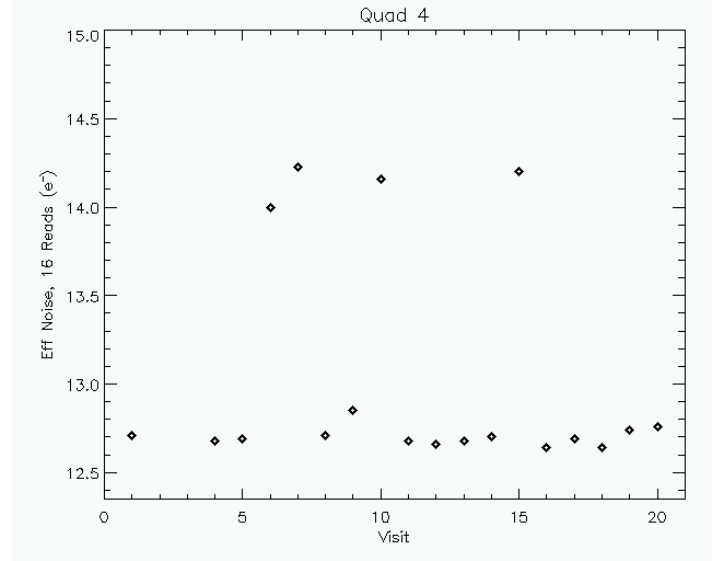


Figure 18: Zoomed out view of quadrant 4 in Figure 16. The effective noise in four of the Visits fails to average down in the same way as the others.

Figures 19 and 20 show similar effective noise plots for the RAPID ramps in this proposal. These RAPID ramps contained only 6 reads, limiting the effective noise measurements compared to those from the SPARS200 ramps. However, with two ramps per Visit, these data gave a large dataset with which to work. Figure 19 shows the effective noise when using all 6 reads in each ramp to create the final image. Table 2 lists the sigma clipped mean and standard deviation of these values. Figure 20 shows how the mean value of the noise averages down versus number of reads. Effective noise values from matching ramps in TV3 are also shown in Table 2. As was seen in the IR Functional Test (Hilbert 2009), the effective noise measured in ground testing was lower than that measured on orbit.

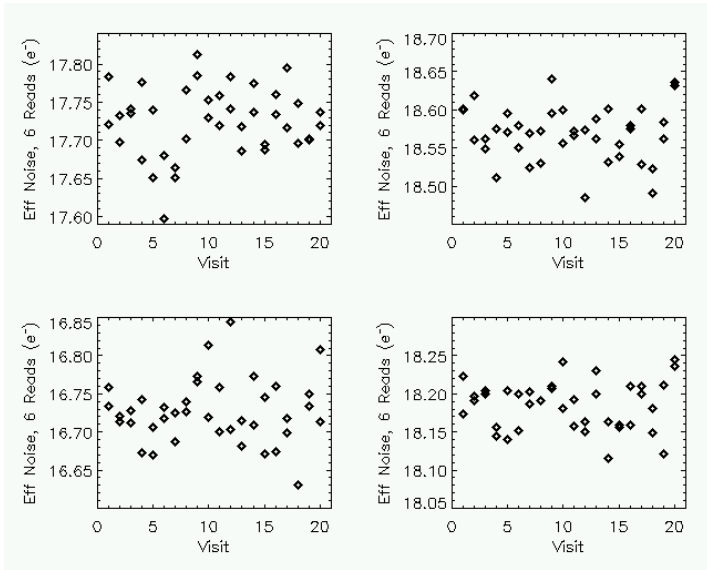


Figure 19: Effective noise values using all 6 reads in each of the 40 RAPID ramps in this proposal.

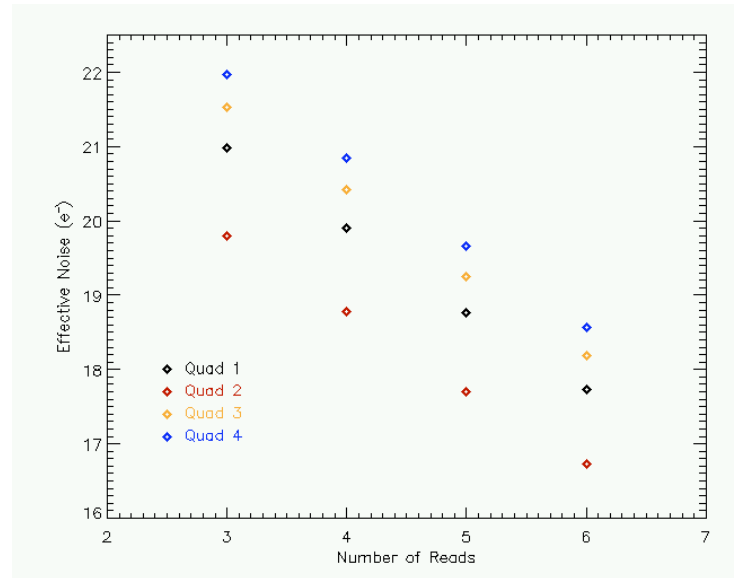


Figure 20: Effective noise versus the number of reads in the RAPID ramps. In this case the RAPID ramps had only 6 reads, limiting us to less than the possible 16 reads explored for the SPARS200 ramps. Note that in this case, using 3 reads provides no reduction in noise compared two reads (CDS noise values in Table 1).

	Quad 1	Quad 2	Quad 3	Quad 4
SMOV	12.18 +/- 0.06	11.60 +/- 0.06	12.50 +/- 0.06	12.69 +/- 0.03
TV3	14.4 +/- 0.1	14.1 +/- 0.1	15.1 +/- 0.1	15.0 +/- 0.1
SMOV RAPID 6	17.73 +/- 0.04	16.72 +/- 0.04	18.19 +/- 0.03	18.57 +/- 0.04
TV3 RAPID 6	16.8 +/- 0.2	16.5 +/- 0.2	17.7 +/- 0.2	18.5 +/- 0.2

Table 2: Sigma-clipped effective readnoise values on a final image constructed using all reads in the ramps (16 reads for SPARS200 and 6 reads for RAPID). Uncertainties are the robust standard deviation of the effective noise values in the individual ramps. TV3 values have been converted to SMOV gain values for a more direct comparison. Values measured with these data are statistically identical to those measured in SMOV proposal 11420 (Hilbert, 2009).

Dark Current

One of the main analysis tasks for this dataset was the calculation of the IR dark current rate. During normal CALWF3 processing, dark current will be subtracted from IR observations using a 15-read mean dark ramp with a sample sequence that matches that of the observation. While creation of these mean dark ramps is the most important product from dark current observations, we also wish to monitor the overall dark current rate of the IR detector, in order to provide a basic characterization of dark current performance.

We used CALWF3-processed *flt* files for our dark current examination. These files have had line-fitting performed to the dark current signal up the ramp for each pixel, in order to determine the dark current rate. The black curve in Figure 21 shows a histogram of one quadrant of a typical dark current image. In order to determine mean dark current rates, we created a histogram for each quadrant of each SPARS200 image. The histograms were fit with a Gaussian, and the peak value of the fit was returned as the “mean” dark rate for that quadrant. In order to get a good fit, we excluded the high dark current tail seen in Figure 21. This tail is consistent with those obtained from ground testing data (Hilbert 2008c).

The red curve in Figure 21 shows the cumulative distribution of the dark current for this quadrant. This shows the percentage of pixels with dark current less than the value on the X axis. For example, approximately 80% of the pixels have a dark current less than 0.06 e⁻/sec. The CEI Specification for IR dark current states that the dark current in the IR channel should be less than 0.4 e⁻/sec/pixel. From the Visit 11 ramp used to generate Figure 21, we find that for this quadrant, approximately 1.4% of the pixels have dark current values that are 0.4 e⁻/sec or higher. Further analysis of various flavors of anomalous pixels is presented in the next section.

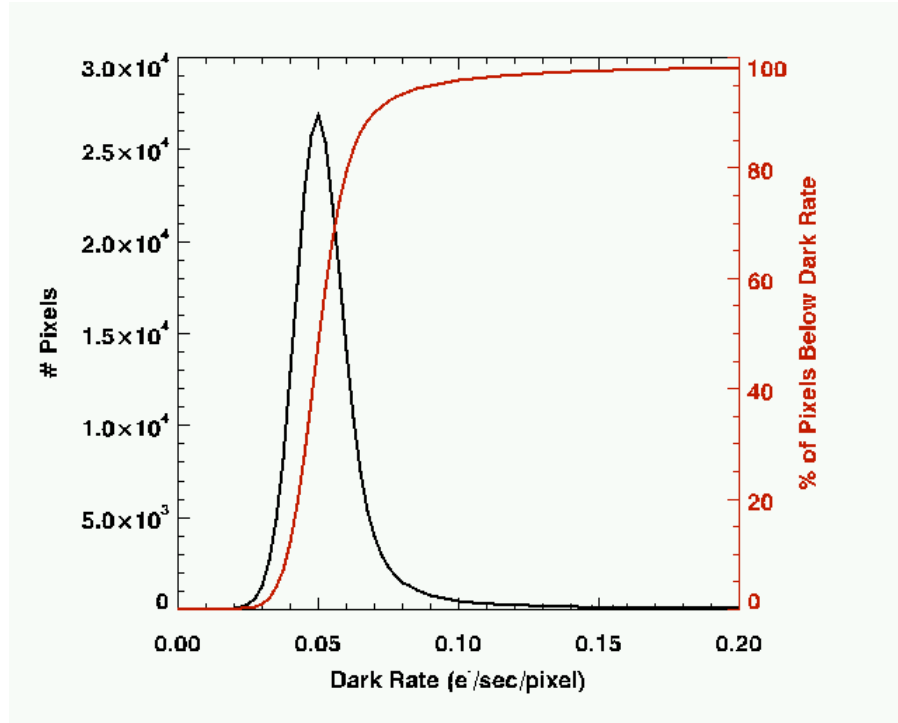


Figure 21: Dark current histogram and cumulative distribution curve for quadrant 1 of the SPARS200 ramp from Visit 11.

After creating histograms and Gaussian fits to all of the SPARS200 ramps in this proposal, we arrived at the dark current values shown in Figure 22. As seen in Figure 13, Visits 4, 8, and 19 show higher-than-expected dark rates. Visit 13 also shows above average dark current. With no IR observations for at least 62 hours prior to Visit 13, the source of this elevated dark current is unknown. Visit 9 shows lower-than-expected dark current. Again, the cause of this is unknown. Visit 9 of the IR Channel Functional Test (proposal number 11420) also showed anomalously low dark current, primarily in quadrants 1 and 2. Further investigation may reveal the source of the low dark current.

Table 3 lists the sigma-clipped mean dark current in each quadrant of the detector, using the values shown in Figure 22. These values are 0.015 – 0.025 e⁻/sec/pixel lower than those seen in TV3 testing.

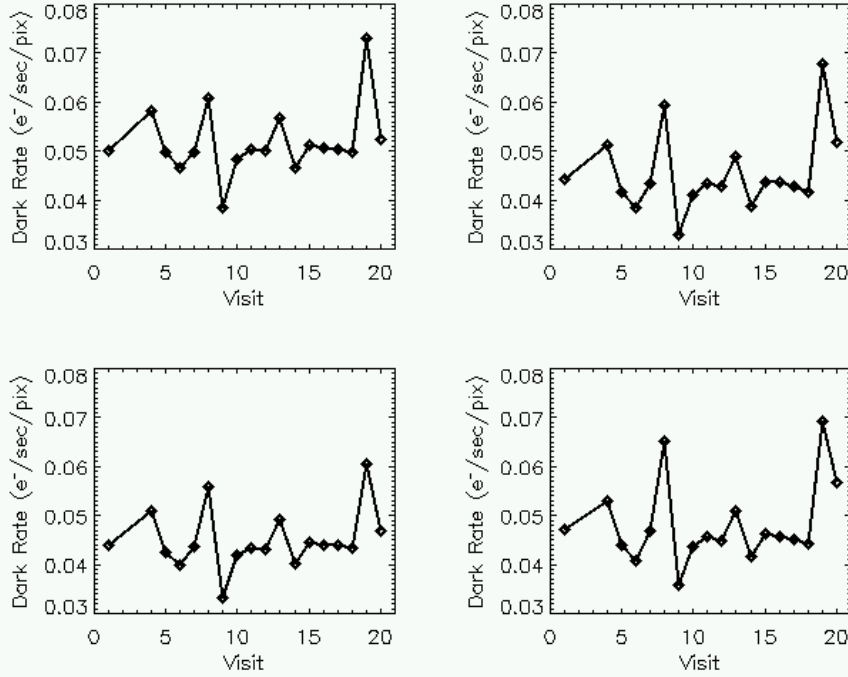


Figure 22: Mean dark current values for the SPARS200 ramps in this proposal. These dark rates were calculated by fitting to the peak of a histogram of the dark current in each of the flt files. The high dark current values in Visits 19 and 8 are due to persistence from internal flat field observations taken 25 minutes and 2 hours prior to the dark current ramp, respectively. Visit 4 took place approximately 40 minutes after observations of an open cluster, suggesting persistence is present. HST was also pointed down at the night side of the Earth during Visit 4. No IR observations were made for approximately 62 hours prior to Visit 13. The reason for the elevated dark current measurements here is unknown.

	Quad 1	Quad 2	Quad 3	Quad 4
SMOV	0.050 +/- 0.003	0.044 +/- 0.004	0.046 +/- 0.005	0.043 +/- 0.005
TV3	0.060 +/- 0.005	0.054 +/- 0.005	0.062 +/- 0.005	0.058 +/- 0.005

Table 3: Mean dark current in $e^-/\text{sec}/\text{pixel}$ measured using all of the SPARS200 ramps from this proposal except for Visits 2 and 3. Dark current rates were determined using a Gaussian fit to the dark rates in each quadrant of each ramp. We then calculated the sigma-clipped mean value for each quadrant. Listed uncertainties are the sigma-clipped standard deviation of the dark rates for all input ramps. TV3 values were taken from Table 3 in Hilbert (2008), and converted to the SMOV gain values mentioned previously.

As with the measured bias levels, we also searched for correlations between the dark current rate and input voltage and FPA temperature. For this analysis we needed measures of the dark current between all consecutive reads within a ramp. For each ramp, we used the 15 reads to create 14 difference images. In each difference image, we calculated the sigma-clipped mean of the signal, and divided this by 200 seconds, which is the time between reads in a SPARS200 ramp.

We first plotted these dark rates against the bus voltage level input to WFC3 from HST. A typical plot is shown in Figure 23, where the input voltage values are shown in red and the dark current values are shown in black. There is no obvious correlation between the two curves in this plot. Also, as shown in Figure 24, we plotted the measured dark rate against the first derivative of the voltage, as a check to see whether abrupt changes in voltage affected the dark current more than the overall voltage level. While there is a suggestion in Figure 24 of a relationship between the two values, an examination of all dark current versus voltage change plots indicate no clear relationship between the two.

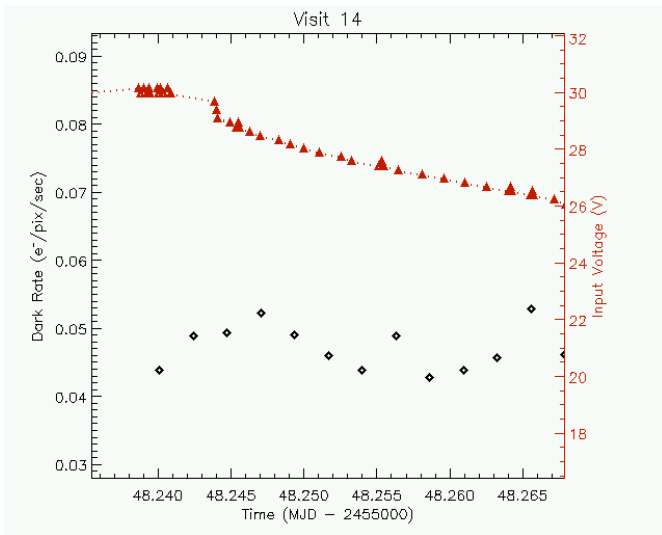


Figure 23: Mean instantaneous dark rate for the Visit 14 SPARS200 ramp, along with input voltages.

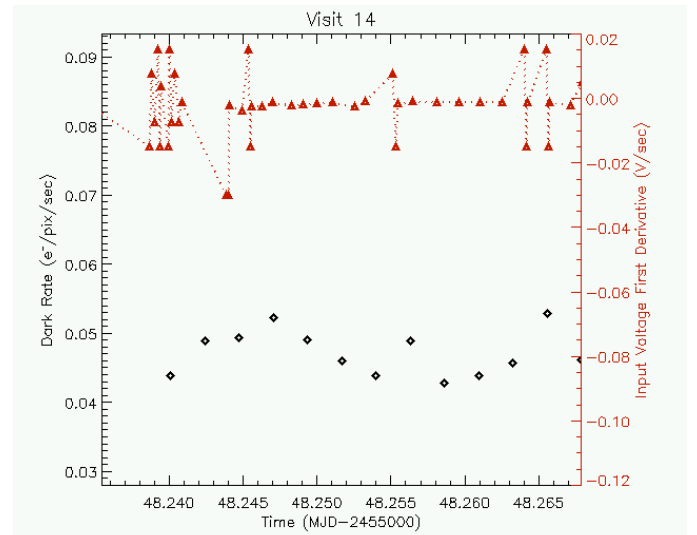


Figure 24: Same as Figure 23, but looking at the change in voltage with time.

The results are much the same from the comparison of dark current level and FPA temperature. Figure 25 shows the measured dark current plotted against the temperature of the FPA, while Figure 26 shows the dark current plotted against the change in FPA temperature. As with the voltage plots, these plots do not reveal any clear relationship between the dark current and FPA temperature. Some plots showed dark current variations that approximately lined up with temperature changes, while others revealed similar dark current variations while the detector temperature was constant. As with the bias comparison to temperature, we are working with temperature values that are varying above and below a single resolution element of the thermistor, which limits the information available to us.

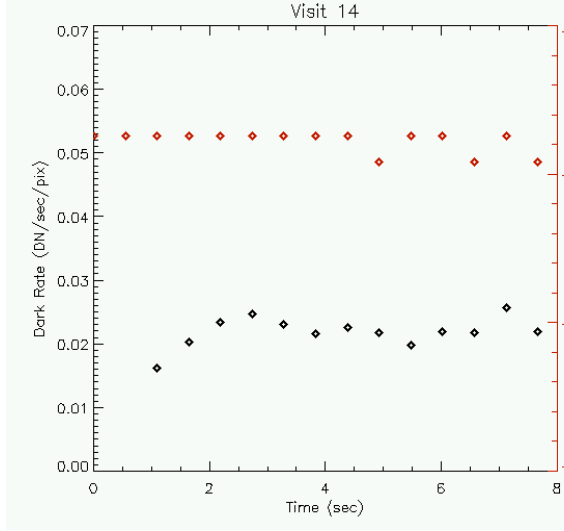


Figure 25: Plot showing the dark current up the ramp for a single SPARS200 ramp (black), plotted against the FPA temperature of the detector (red).

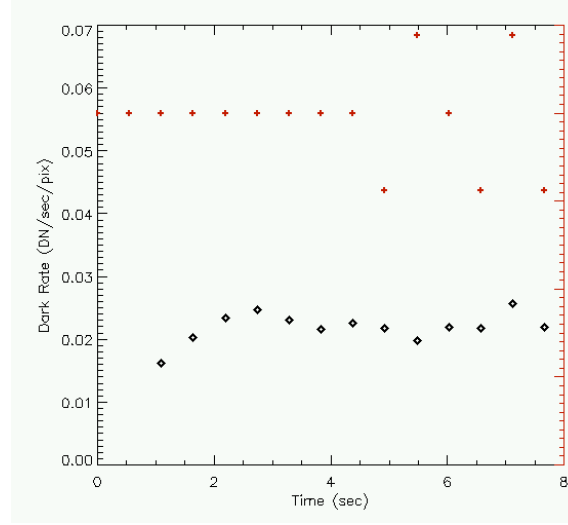


Figure 26: Plot showing the dark current up the ramp for a single SPARS200 ramp (black), plotted against the change in FPA temperature with time (red).

Bad Pixels

We also investigated statistics on anomalous pixels in the IR detector. Table 4 shows the SMOV statistics are similar to those previously measured during TV3 and reported by Hilbert (2008), also from SPARS200 ramps, the longest SPARS sample sequence, which gives good signal to noise for the dark current and hence yields the most accurate count of anomalous pixels. Not only are the statistics of anomalous pixels similar in SMOV as TV3, the vast majority of the anomalous pixels are indeed the very same pixels in the two circumstances. That is, the detector is exhibiting similar behavior now in orbit as it did on the ground; it appears that launching the instrument has not created a large number of “new” bad pixels, nor miraculously fixed any large number of “old” bad pixels.

Percentage of Non-nominal Pixels MEB2: SMOV/TV3				
	Above CEI	Hot Pixels	Dark Pixels	Negative Pixels
SPARS200				
Quad 1	0.9 / 1.0	0.6 / 0.6	0.02 / 0.03	0.5 / 0.4
Quad 2	0.7 / 0.7	0.4 / 0.4	0.03 / 0.01	0.07 / 0.04
Quad 3	0.5 / 0.5	0.3 / 0.3	0.02 / 0.01	0.07 / 0.04
Quad 4	0.6 / 0.6	0.3 / 0.3	0.02 / 0.02	0.2 / 0.2

Table 4: Fraction of light-sensitive pixels with non-nominal behaviors. All from SPARS200 data; pairs of elements are presented as “SMOV value / TV3 value” each in percent. TV3 values are from Hilbert 2008. The first column represents pixels with dark current values greater than the CEI Spec value of $0.4 \text{ e}^-/\text{sec/pixel}$. The hot pixel column is for those pixels with dark current greater than $1.0 \text{ e}^-/\text{sec/pixel}$. Dark pixels are those with dark current less than $0.01 \text{ e}^-/\text{sec/pixel}$ and greater than zero, and negative pixels are those with dark current values less than $0 \text{ e}^-/\text{sec/pixel}$.

Cosmic Rays

Finally, we performed a comparison of the measured cosmic ray rates between ground testing and on-orbit testing. Using the SPARS200 dark ramps from this proposal, we relied on CALWF3’s ability to detect cosmic rays during normal processing. Using the data quality arrays for each of the SPARS200 ramps, we were able to calculate the total number of cosmic rays incident upon the detector. We also recorded the intensity of each cosmic ray, and built up a histogram of those values. Figure 27 shows this histogram for one of the SMOV SPARS200 ramps, while Figure 28 shows the same histogram for a SPARS200 ramp collected during ground testing. The two histograms appear qualitatively similar in terms of peak intensity and the shape of the tail of the distribution.

Table 5 also gives the mean number of cosmic rays identified per ramp along with the standard distribution. As expected, the number of cosmic rays observed during ground testing was much lower than that on orbit. This is due to the shielding provided by the Earth’s atmosphere and the thermal vacuum chamber. The cosmic ray rate on orbit is between 5.8 and 7.9 times that observed on the ground.

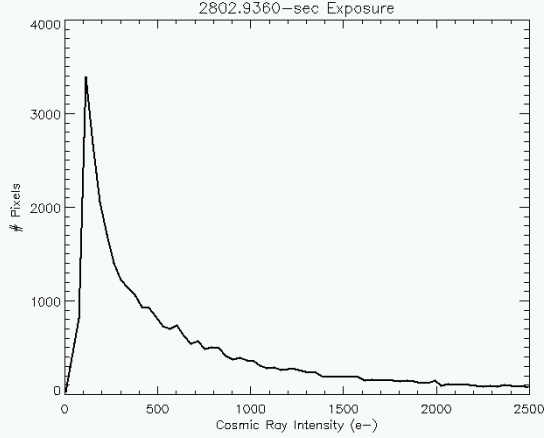


Figure 27: Cosmic ray intensity histogram from Visit 4 SPARS200 ramp.

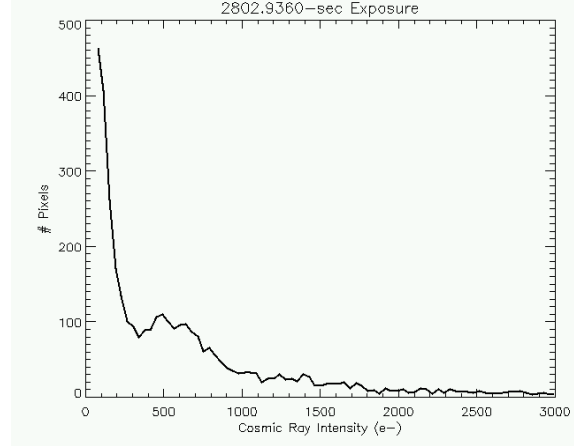


Figure 28: Cosmic ray intensity histogram for a TV3 SPARS200 ramp.

	Mean Total Cosmic Rays	Robust Stdev	CRs per sec	CRs per sec per cm ²
SMOV	30700	4150	11 +/- 1.5	3.2 +/- 0.4
TV3	3975	46	1.4 +/- 0.02	0.42 +/- 0.01
TV3 spars100	2690	47	1.9 +/- 0.03	0.56 +/- 0.01

Table 5: Mean and standard deviation of the number of cosmic rays identified by CALWF3. For SMOV, all data were SPARS200 ramps. For TV3, we used three SPARS200 and three SPARS100 ramps. The cause behind the difference in cosmic ray rate between the ground SPARS200 and ground SPARS100 ramps is unclear. CALWF3 settings were identical for all three datasets and are described in the Appendix. In order to translate between the cosmic ray rate on the detector and that per cm², we use an area of 3.40 cm² for the IR focal plane.

IR Background

Visit 33 measured sky backgrounds in the Anti-Sun direction on Jul 19, 2009. HST was flying above the twilight or dark Earth and the Moon was nearly new, so scattered Earthlight and scattered Moonlight should not contribute to the background.

Visit 34 measured sky backgrounds in the HST orbit-pole direction on the same day. In that case, Earth-shine is very significant (as discussed and illustrated in this report). As evident from Table 2b, for each filter, the Visit 33 measurement (toward the Anti-Sun direction) is approximately 20% greater than the faintest (zero Earthshine) Visit 34 background (toward the HST orbit pole). This is expected, since the Anti-Sun direction is in the ecliptic plane and further enhanced by its 180 degree solar elongation (i.e. looking at the Gegenschein).

We do not expect backgrounds in Visit 33 to be contaminated by Earthshine, because for most of the time, the limb angle was much larger than 24 degrees, and also HST was

flying above the dark Earth nearly all the time - only briefly above twilight Earth. In summary of Visit 33, the observed backgrounds in the wide (W) filters are 1.7 times the ETC estimates using zero Earthshine, as appropriate for the conditions of Visit 33. The associated medium (M) band filters have a ratio of 1.4 between observed and ETC estimates. In each case, the ratio (observed/ETC) deviates from unity slightly more at shorter wavelengths. When compared to the instrument handbook (IHB), the observed values are 1.4 and 1.3 times greater than those given in Table 7.12, although this comparison is both ad hoc and presumably inappropriate because the IHB estimate contains a nominal Earthshine value, whereas we expect it to be nearly zero for the conditions of the observations of Visit 33. (Complicating matters is the IHB's description of Table 7.12 – it doesn't mention the method of estimating the Earthshine; also in the IHB, Table 9.3's Earthshine values are said to be "high" and correspond to limb angle 38 degrees (on p. 145), but elsewhere (on p. 147) are said to be for 24 degrees (as appropriate for the CVZ)). From point-source photometry in SMOV, we know that the total throughput of WFC3 IR is approximately 20% greater than predicted; hence, some of the enhancement in the observed background (compared to pre-SMOV predictions discussed here) is also attributable to that same 20%.

Backgrounds in Visit 34 are contaminated by an unexpected spatially-variable component which is apparently Earthshine. The left side of the array (approximately the first 200 columns of light-sensitive pixels) exhibits a variable brightness even greater than the variability of the rest of the array. The left side is brighter than the rest of the array (Figure 33) in the two-orbit sequence (Figure 29), repeatedly in orbital phase when the HST is at a particular orientation to the bright Earth (see Figure 30).

We expect Earthshine to be time-variable (due to different terrain, oceans, clouds) and wavelength dependent (primarily due to the solar spectrum decreasing with increasing wavelength, and water vapor absorption at 1.4 microns – see LCROSS spectra of Earth in McCullough 2009 analysis of brightness of Earthshine and ocean glints). The coupling of Earthshine to the HST is strongly dependent on the angle subtended from the HST's pointing direction (so called "V1" direction) and the nearest limb of the Earth; that angle is called the "limb angle" for short. However, to our knowledge, no other HST instrument has exhibited a spatial variation in the Earthshine similar to WFC3 IR as shown in Figure 33. We speculate that the refractive corrector plate's lens element is imaging stray light upon the IR sensor that did not follow the intended path through the other optics. In this scenario, the RCP's lens does not produce an in-focus image of the surface of last scattering of the stray light because the object distance is so small.

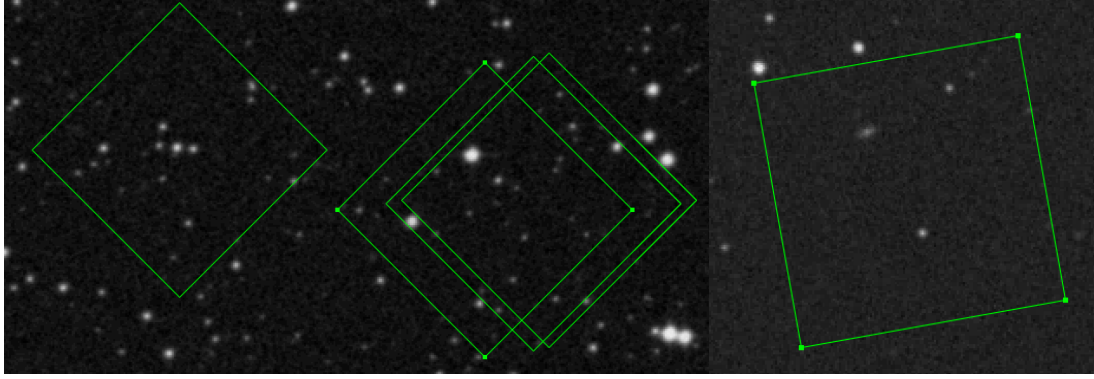


Figure 29: Digital Sky Survey images with approximate sizes and orientations of the WFC3 IR field of view superposed. North is up, East to the left. Visit 33 (left) is aimed at the anti-Sun, $(RA, DEC) [2000] = (298.40, -20.87)$, Galactic $(l, b) = (20.23, -22.6)$, and ecliptic $(296.39, 0.00)$. The pointing drifted eastward, i.e. to the left, as shown by the four boxes corresponding to exposures 1, 2, 6, and 9 of Visit 33. Visit 34 (right) is aimed at the orbit pole, $(RA, DEC) [2000] = (162.16, +61.55)$, Galactic $(l, b) = (145.14, +49.95)$, and ecliptic $(133.16, +48.47)$. The scale of the drift was less in Visit 34 than Visit 33. The coordinates in the `_raw.fits` (etc) files are correct for Visit 33 but incorrect for Visit 34; for the latter, the jitter files `_jif.fits` give approximately correct coordinates.

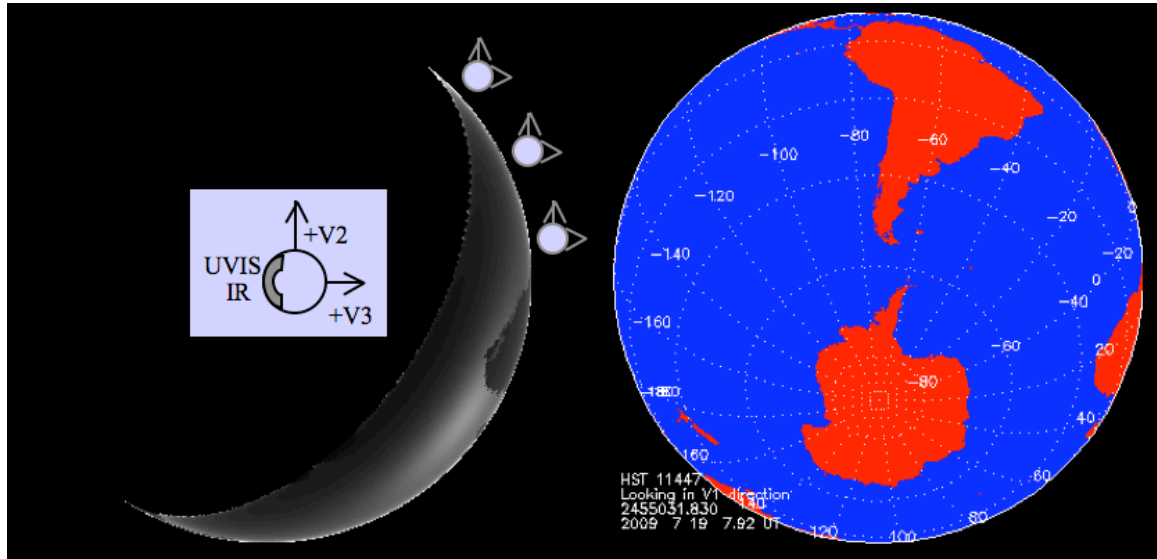


Figure 30: A model of the solar illumination on the Earth (left) and a map (right) during Program 11447's Visit 34. HST orbits 1.088 times the radius of the Earth from the center of each diagram in a counter-clockwise direction; three diagrams of HST are shown, at the locations of three consecutive exposures that exhibit additional stray light in the left ~200 columns of quadrants 1 and 2 of the IR sensor, specifically in exposures `iabz34xxx` with `xxx = s0q, s2q, s4q`. For both diagrams, the viewer is at infinity in the $-V1$ direction, i.e. the viewer is looking in the same vector direction as HST but looking at the Earth. Because Visit 34's target $(RA, DEC) = (162, +62)$ was the (northern) orbital pole, the orbital plane of HST is in the plane of the paper, i.e. the $V2$ - $V3$ plane also equals the plane of the paper (inset diagram at left). The (RA, DEC) of $V2$ and $V3$ are $(19, +24)$ and $(102, -15)$, respectively, hence $V2$ and $V3$ are approximately up and right, respectively. The locations of WFC3's UVIS and IR sides of the instrument are indicated. The Sun is located at $(RA, DEC) = (119, +21)$, approximately at 4 O'clock on the diagrams, evident from the glint of sunlight off the Atlantic near South Africa.

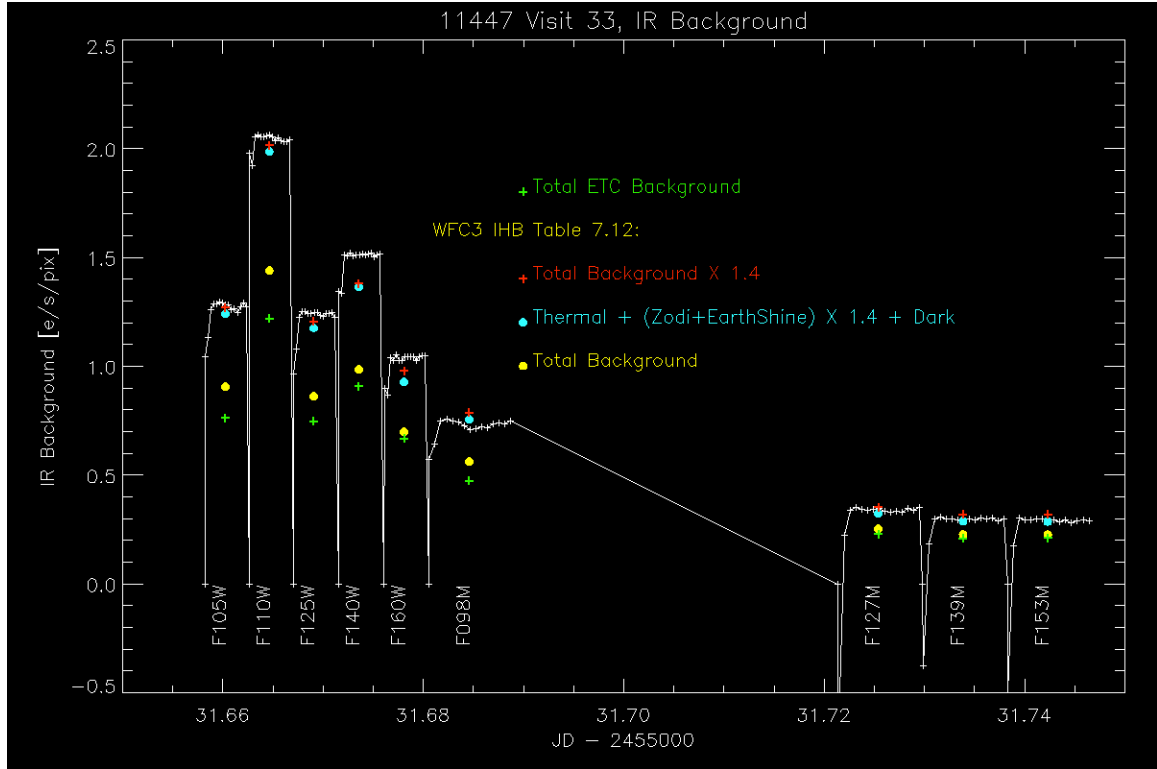


Figure 31: Brightness versus time for Visit 33. HST was pointed at the anti-solar direction, i.e. the Genshein. Individual forward differences of the MULTIACCUM sequences are plotted, in electrons per second per pixel. We used a robust mean, i.e. with outlier rejection, of the nearly isotropic brightness over the entire 1014x1014 IR array, with (almost negligible) reference pixel subtraction. Background estimates for each filter are also plotted: the Exposure Time Calculator (ETC) estimates (green + symbols) tend to be less than the estimates from Table 7.12 of the Instrument Handbook (IHB, yellow circles). The ETC estimates given here have zero Earthshine contribution, whereas the IHB values include a nominal Earthshine contribution. Two ad hoc comparisons to the IHB are also plotted (red + symbols and light blue circles – see legend). The medians of each exposure are tabulated separately along with the ETC and IHB estimates.

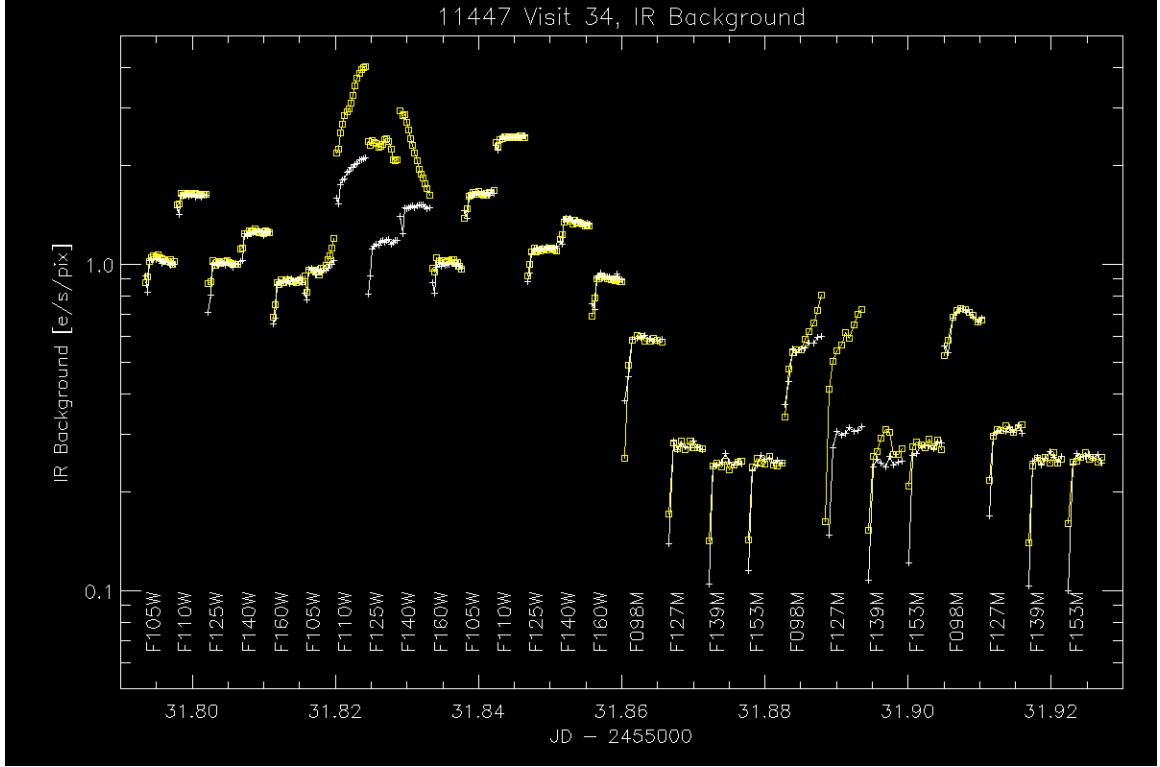


Figure 32: Brightness versus time for Visit 34. Similar to the previous figure, individual forward differences of the MULTIACCUM sequences are plotted, in electrons per second per pixel. In this visit, HST was pointed at the HST orbit pole and hence had a (nearly) constant 23.5 (check that) degree angle to the nearest limb of the Earth. Consequently, as expected, earthshine is bright and time variable, but unexpectedly it is also quite variable with position on the IR array. We plot two robust means, i.e. with outlier rejection, of the nearly isotropic brightnesses within two regions of the 1024x1024 IR array: (white + symbols) columns 512-712, and (yellow squares) columns 5 to 204. Again, we performed reference pixel subtraction but doing so makes hardly any difference. Evidently, the left or first ~200 columns of the IR array are susceptible to as much as ~2x greater background stray light as the rest of the array (see Figure 5). The medians of each exposure are tabulated separately along with the ETC and IHB estimates.



Figure 33: Anomalous stray light from Earthshine. In some exposures of Visit 34 (see Figure 32), the left or first ~200 columns of the IR array are susceptible to as much as ~2x greater background stray light as the rest of the array. The arc-shaped edge between the extra stray light extends from the top of the sensor at column ~200 down across the “death star” feature in quadrant 2; this arc-shape edge is constant in shape and position for all cases in which the anomalous stray light appears, although its overall brightness changes. (Trailed stars are also visible as white streaks.)

Backgrounds in Visit 33 (HST aimed at Anti-Sun)

Background irradiances on the WFC3 IR array are tabulated below, first in chronological order from exposure I=1 to 9. We tabulate the robust (i.e. with outlier rejection) mean irradiance of the array in electrons/s/pix for a nominal gain of 2.5 e/DN. (Unlike Visit 34, in Visit 33, the irradiance is uniform across the array, consistent with the expected negligible Earthshine contribution in Visit 33.) The Exposure Time Calculator (ETC) estimates tend to be less than the estimates from Table 7.12 of the Instrument Handbook (IHB), in part because the ETC estimates given here have zero Earthshine contribution, whereas the IHB values include an Earthshine contribution.

I	Filter	Obs (e/s/pix)	IHB	ETC	Obs/IHB	Obs/ETC
1	F105W	1.275	0.905	0.761	1.408	1.675
2	F110W	2.052	1.438	1.217	1.427	1.686
3	F125W	1.242	0.860	0.746	1.445	1.666
4	F140W	1.511	0.985	0.906	1.534	1.668
5	F160W	1.043	0.697	0.665	1.496	1.568
6	F098M	0.734	0.560	0.471	1.310	1.558
7	F127M	0.339	0.251	0.227	1.349	1.492
8	F139M	0.297	0.226	0.207	1.313	1.433
9	F153M	0.293	0.226	0.210	1.295	1.394

Table 6: Background signal levels.

Backgrounds in Visit 34 (HST aimed at Orbit Pole)

Background irradiances on the WFC3 IR array are tabulated below, first in chronological order from exposure I=1 to 27 (Table 7), then arranged by filter to better see temporal variations (Table 8). In the latter arrangement, for comparison we append the Visit 33 measurements and precede each with an asterisk. For the Visit 34 data, we tabulate the robust (i.e. with outlier rejection) mean irradiance of columns 5 to 204 (B1), columns 512 to 711 (B2) and their ratio (B1/B2). B1 and B2 are in electrons/s/pix for a nominal gain of 2.5 e/DN. Variability of results for a given filter is attributable to variations in Earthshine incident upon the array.

I	Filter	B1	B2	B1/B2
1	F105W	1.029	1.018	1.011
2	F110W	1.634	1.620	1.008
3	F125W	1.007	0.998	1.009
4	F140W	1.255	1.248	1.006
5	F160W	0.881	0.882	0.999
6	F105W	0.959	0.960	0.999
7	F110W	3.120	1.974	1.580
8	F125W	2.320	1.163	1.994
9	F140W	2.194	1.491	1.471
10	F160W	1.019	0.993	1.027
11	F105W	1.638	1.638	1.000
12	F110W	2.443	2.543	0.996
13	F125W	1.103	1.115	0.989
14	F140W	1.333	1.342	0.993
15	F160W	0.899	0.907	0.991
16	F098M	0.582	0.588	0.990
17	F127M	0.272	0.274	0.990
18	F139M	0.240	0.243	0.990
19	F153M	0.242	0.245	0.989
20	F098M	0.548	0.551	0.995
21	F127M	0.566	0.302	1.871
22	F139M	0.262	0.242	1.082
23	F153M	0.275	0.272	1.010
24	F098M	0.685	0.683	1.004
25	F127M	0.309	0.306	1.011
26	F139M	0.246	0.249	0.986
27	F153M	0.249	0.254	0.979

Table 7: Background irradiances, in chronological order.

I	Filter	B1	B2	B1/B2
20	F098M	0.548	0.551	0.995
16	F098M	0.582	0.588	0.990
24	F098M	0.685	0.683	1.004
*	F098M	0.734		
6	F105W	0.959	0.960	0.999
1	F105W	1.029	1.018	1.011
11	F105W	1.638	1.638	1.000
*	F105W	1.275		
2	F110W	1.634	1.620	1.008
12	F110W	2.443	2.453	0.996
7	F110W	3.120	1.974	1.580
*	F110W	2.052		
3	F125W	1.007	0.998	1.009
13	F125W	1.103	1.115	0.989
8	F125W	2.320	1.163	1.994
*	F125W	1.242		
17	F127M	0.272	0.274	0.990
25	F127M	0.309	0.306	1.011
21	F127M	0.566	0.302	1.871
*	F127M	0.339		
18	F139M	0.240	0.243	0.990
26	F139M	0.246	0.249	0.986
22	F139M	0.262	0.242	1.082
*	F139M	0.297		
4	F140W	1.255	1.248	1.006
14	F140W	1.333	1.342	0.993
9	F140W	2.194	1.491	1.471
*	F140W	1.511		
19	F153M	0.242	0.245	0.989
27	F153M	0.249	0.254	0.979
23	F153M	0.275	0.272	1.010
*	F153M	0.293		
5	F160W	0.881	0.882	0.999
15	F160W	0.899	0.907	0.991
10	F160W	1.019	0.993	1.027
*	F160W	1.043		

Table 8: Background irradiances, filter by filter.

Conclusions

The IR Channel in WFC3 during SMOV performs essentially as it did during TV3. Average dark current and CDS read noise measured in SMOV (available in the abstract and Tables 3 and 1) are similar to those measured in TV3. Further dark current and readnoise monitoring will be performed using the Cycle 17 dark monitoring program (11929). The spatial distribution, i.e. the 2-D pattern, of dark current (Figure 3) is similar to that observed in TV3. The anomalous pixel population is appears largely unchanged from TV3 to SMOV (Table 4). The on-orbit measured cosmic ray rate approximately 11 hits per second on the detector. This is 6 to 8 times higher than that observed in the thermal vacuum testing chamber.

Unresolved Issues

The decrease in zeroth read signal with time seen in Figure 9 is not understood. Further monitoring of this signal level seems necessary.

Also, close monitoring of the signal in the final read of a set of nominally ramps seems necessary. The variation seen in the read 15 signal levels of the SPARS200 darks in this data set was larger than expected.

The effects of persistence on these data are obvious, even in ramps taken 2 hours after an internal flat field. A full characterization of the persistence behavior is necessary.

The high effective noise values in quadrants 3 and 4 observed in some of the SPARS200 ramps are not well understood. Further analysis is necessary.

References

- Hilbert, B., (2008a) *WFC3 TV2 Testing: IR Channel Dark Current*. WFC3 ISR 2008-03. <http://www.stsci.edu/hst/wfc3/documents/ISRs/WFC3-2008-03.pdf> Jan 2008.
- Hilbert, B., (2008b) *WFC3 TV3 Testing: IR Channel Read Noise*. WFC3 ISR 2008-25. <http://www.stsci.edu/hst/wfc3/documents/ISRs/WFC3-2008-25.pdf> July 2008.
- Hilbert, B., (2008c) *WFC3 TV3 Testing: IR Channel Dark Current*. WFC3 ISR 2008-30. <http://www.stsci.edu/hst/wfc3/documents/ISRs/WFC3-2008-30.pdf> Sept 2008.
- Hilbert, B. and P. McCullough, (2009) *WFC3 SMOV Testing: IR Channel Functional Tests*. WFC3 ISR 2009-23. <http://www.stsci.edu/hst/wfc3/documents/ISRs/WFC3-2009-23.pdf> November 2009.
- McCullough, P., (2009) *Tools for predicting HST's orientation with respect to Earth*. WFC3 ISR 2009-xx. In press.

Appendix

Table 9 lists the details of the observations made as part of program 11447.

Visit	Filename	Sample Sequence /NSAMP	Exposure Time (sec)	Target	Filter
1	iabz01oiq	RAPID / 6	14.66	Dark	Blank
2	iabz02b8q	RAPID / 6	14.66	Dark	Blank
3	iabz03shq	RAPID / 6	14.66	Dark	Blank
4	iabz04p1q	RAPID / 6	14.66	Dark	Blank
5	iabz05xpq	RAPID / 6	14.66	Dark	Blank
6	iabz06gdq	RAPID / 6	14.66	Dark	Blank
7	iabz07awq	RAPID / 6	14.66	Dark	Blank
8	iabz08oiq	RAPID / 6	14.66	Dark	Blank
9	iabz09ecq	RAPID / 6	14.66	Dark	Blank
10	iabz10ggq	RAPID / 6	14.66	Dark	Blank
11	iabz11abq	RAPID / 6	14.66	Dark	Blank
12	iabz12d3q	RAPID / 6	14.66	Dark	Blank
13	iabz13leq	RAPID / 6	14.66	Dark	Blank
14	iabz14liq	RAPID / 6	14.66	Dark	Blank
15	iabz15h6q	RAPID / 6	14.66	Dark	Blank
16	iabz16h3q	RAPID / 6	14.66	Dark	Blank
17	iabz17q2q	RAPID / 6	14.66	Dark	Blank
18	iabz18stq	RAPID / 6	14.66	Dark	Blank
19	iabz19e1q	RAPID / 6	14.66	Dark	Blank
20	iabz20u0q	RAPID / 6	14.66	Dark	Blank
1	iabz01ojq	SPARS200 / 15	2802.94	Dark	Blank
2	iabz02b9q	SPARS200 / 15	2802.94	Dark	Blank
3	iabz03siq	SPARS200 / 15	2802.94	Dark	Blank
4	iabz04p2q	SPARS200 / 15	2802.94	Dark	Blank
5	iabz05xqq	SPARS200 / 15	2802.94	Dark	Blank
6	iabz06geq	SPARS200 / 15	2802.94	Dark	Blank
7	iabz07axq	SPARS200 / 15	2802.94	Dark	Blank
8	iabz08ojq	SPARS200 / 15	2802.94	Dark	Blank
9	iabz09edq	SPARS200 / 15	2802.94	Dark	Blank
10	iabz10ghq	SPARS200 / 15	2802.94	Dark	Blank
11	iabz11acq	SPARS200 / 15	2802.94	Dark	Blank

12	iabz12d4q	SPARS200 / 15	2802.94	Dark	Blank
13	iabz13lfq	SPARS200 / 15	2802.94	Dark	Blank
14	iabz14ljq	SPARS200 / 15	2802.94	Dark	Blank
15	iabz15h7q	SPARS200 / 15	2802.94	Dark	Blank
16	iabz16h4q	SPARS200 / 15	2802.94	Dark	Blank
17	iabz17q3q	SPARS200 / 15	2802.94	Dark	Blank
18	iabz18suq	SPARS200 / 15	2802.94	Dark	Blank
19	iabz19e2q	SPARS200 / 15	2802.94	Dark	Blank
20	iabz20u1q	SPARS200 / 15	2802.94	Dark	Blank
1	iabz01okq	RAPID / 6	14.66	Dark	Blank
2	iabz02baq	RAPID / 6	14.66	Dark	Blank
3	iabz03sjq	RAPID / 6	14.66	Dark	Blank
4	iabz04p3q	RAPID / 6	14.66	Dark	Blank
5	iabz05xrq	RAPID / 6	14.66	Dark	Blank
6	iabz06gfq	RAPID / 6	14.66	Dark	Blank
7	iabz07ayq	RAPID / 6	14.66	Dark	Blank
8	iabz08okq	RAPID / 6	14.66	Dark	Blank
9	iabz09eeq	RAPID / 6	14.66	Dark	Blank
10	iabz10giq	RAPID / 6	14.66	Dark	Blank
11	iabz11adq	RAPID / 6	14.66	Dark	Blank
12	iabz12d5q	RAPID / 6	14.66	Dark	Blank
13	iabz13lgq	RAPID / 6	14.66	Dark	Blank
14	iabz14lkq	RAPID / 6	14.66	Dark	Blank
15	iabz15h8q	RAPID / 6	14.66	Dark	Blank
16	iabz16h5q	RAPID / 6	14.66	Dark	Blank
17	iabz17q4q	RAPID / 6	14.66	Dark	Blank
18	iabz18svq	RAPID / 6	14.66	Dark	Blank
19	iabz19e3q	RAPID / 6	14.66	Dark	Blank
20	iabz20u2q	RAPID / 6	14.66	Dark	Blank
33	iabz33r8q	SPARS25 / 16	352.94	ANTI-SUN	F105W
	iabz33r9q	SPARS25 / 16	352.94	ANTI-SUN	F110W
	iabz33rbq	SPARS25 / 16	352.94	ANTI-SUN	F125W
	iabz33rdq	SPARS25 / 16	352.94	ANTI-SUN	F140W
	iabz33rfq	SPARS25 / 16	352.94	ANTI-SUN	F160W
	iabz33rhq	SPARS50 / 16	702.94	ANTI-SUN	F098M
	iabz33rjq	SPARS50 / 16	702.94	ANTI-SUN	F127M
	iabz33rlq	SPARS50 / 16	702.94	ANTI-SUN	F139M
	iabz33rnq	SPARS50 / 16	702.94	ANTI-SUN	F153M
34iabz	iabz34rpq	SPARS25 / 16	352.94	ORBIT-POLE	F105W
	iabz34ryq	SPARS25 / 16	352.94	ORBIT-POLE	F105W
	iabz34s8q	SPARS25 / 16	352.94	ORBIT-POLE	F105W
	iabz34rqq	SPARS25 / 16	352.94	ORBIT-POLE	F110W
	iabz34s0q	SPARS25 / 16	352.94	ORBIT-POLE	F110W

	iabz34saq	SPARS25 / 16	352.94	ORBIT-POLE	F110W
	iabz34rsq	SPARS25 / 16	352.94	ORBIT-POLE	F125W
	iabz34s2q	SPARS25 / 16	352.94	ORBIT-POLE	F125W
	iabz34scq	SPARS25 / 16	352.94	ORBIT-POLE	F125W
	iabz34ruq	SPARS25 / 16	352.94	ORBIT-POLE	F140W
	iabz34s4q	SPARS25 / 16	352.94	ORBIT-POLE	F140W
	iabz34seq	SPARS25 / 16	352.94	ORBIT-POLE	F140W
	iabz34rwq	SPARS25 / 16	352.94	ORBIT-POLE	F160W
	iabz34s6q	SPARS25 / 16	352.94	ORBIT-POLE	F160W
	iabz34sgq	SPARS25 / 16	352.94	ORBIT-POLE	F160W
	iabz34siq	SPARS50 / 11	452.94	ORBIT-POLE	F098M
	iabz34soq	SPARS50 / 11	452.94	ORBIT-POLE	F098M
	iabz34suq	SPARS50 / 11	452.94	ORBIT-POLE	F098M
	iabz34skq	SPARS50 / 11	452.94	ORBIT-POLE	F127M
	iabz34sqq	SPARS50 / 11	452.94	ORBIT-POLE	F127M
	iabz34swq	SPARS50 / 11	452.94	ORBIT-POLE	F127M
	iabz34slq	SPARS50 / 11	452.94	ORBIT-POLE	F139M
	iabz34srq	SPARS50 / 11	452.94	ORBIT-POLE	F139M
	iabz34sxq	SPARS50 / 11	452.94	ORBIT-POLE	F139M
	iabz34snq	SPARS50 / 11	452.94	ORBIT-POLE	F153M
	iabz34stq	SPARS50 / 11	452.94	ORBIT-POLE	F153M
	iabz34szq	SPARS50 / 11	452.94	ORBIT-POLE	F153M
TV3	ii01030lr_08105020957	SPARS200 / 15	2802.94	Dark	Blank
	ii01030nr_08105023340	SPARS200 / 15	2802.94	Dark	Blank
	ii01030qr_08105030325	SPARS200 / 15	2802.94	Dark	Blank
	ii01030rr_08105035032	SPARS100 / 15	1402.4	Dark	Blank
	ii01030tr_08105043738	SPARS100 / 15	1402.4	Dark	Blank
	ii01030vr_08105052530	SPARS100 / 15	1402.4	Dark	Blank

Table 9: Basic characteristics of the data taken for this proposal. All SMOV filenames listed in the Table can be found in the HST archive with ‘iabz’ pre-pended to the names given. Prior to Visit 5, these data were subject to the light leak described in Hilbert (2009). Files marked in red exhibit light leak effects, and were ignored in subsequent analysis. The file shown in blue shows the effects of persistence from a previous internal flat field observation. This file was also ignored when calculating mean dark current rates. TV3 ramps listed in the final two rows were used for cosmic ray rate comparisons.

Tables 10 and 11 list the reference files used by CALWF3 to process the data collected in proposal number 11447.

File	Filename	Purpose
BPIXTAB	t291659ni_bpx.fits	Bad pixel table
CCDTAB	t2c16200i_ccd.fits	Detector calibration parameters
OSCNTAB	q911321mi_osc.fits	Detector overscan table
CRREJTAB	t3j1659ki_crr.fits	Cosmic ray rejection parameters
DARKFILE	*	Dark current correction ramp
GRAPHTAB	t2605492m_tmg.fits	HST graph table
COMPTAB	t6i1714pm_tmc.fits	HST components table

Table 10: Reference files used for all ramps collected as part of proposal 11447. Darkfile names are listed in the table below, as we have a different dark current calibration file for each sample sequence and subarray size. Files listed in both of these tables can be downloaded from the HST archive.

Sample Sequence	Array Size (pixels)	Dark File for CALWF3
SPARS25	1024 x 1024	
SPARS50	1024 x 1024	t611932ji_drk.fits

Table 11: Dark current correction ramps used by CALWF3 when processing the internal flat field ramps taken as part of proposal 11447.

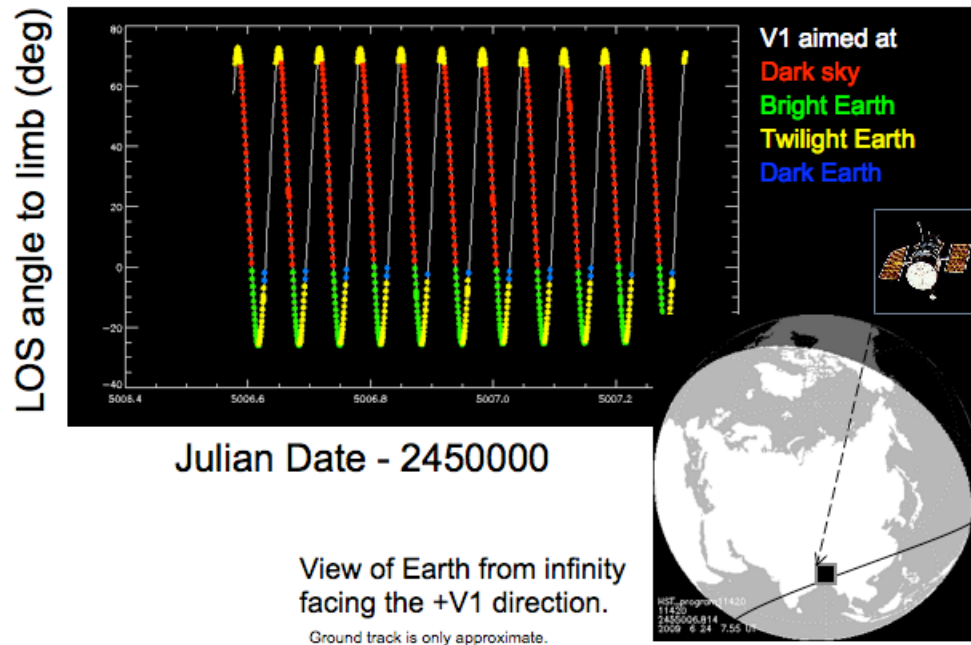


Figure 36: Geometry of Program 11420 of the initial execution on June 24, 2009 of the SPARS200 darks that exhibited a light leak illustrated in the following figures and described in the text. The view of Earth (inset) is from infinity facing the +V1 direction, i.e. facing the same direction as HST. The ground track is approximate and only illustrative of a typical HST pass.

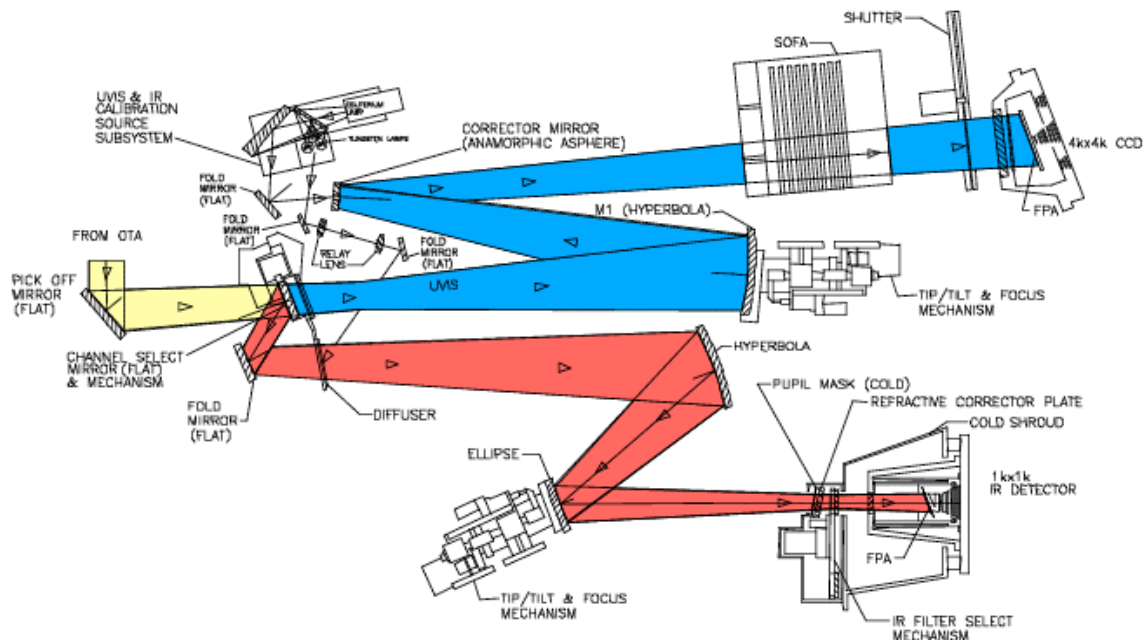


Figure 37: Schematic optical layout of WFC3 from its Instrument Handbook. The IR light leak path hypothesis involves light incident upon IR refractive corrector plate (labeled) scattering off and around the IR filter select mechanism (labeled) and ending its path at the IR focal plane assembly (labeled FPA).